

Low-Dimensional Plasmonic Photodetectors: Recent Progress and Future Opportunities

Jian-An Huang and Lin-Bao Luo*

Plasmonic nanostructures can achieve subdiffraction-limit light confinement with enhanced electric fields. By taking advantage of the light-confinement effect, various plasmonic photodetectors that combine low-dimensional (LD) semiconductor structures and plasmonic materials have recently demonstrated excellent plasmon-enhanced device performance and attracted significant research interest. In this review, the state-of-the-art progress in the development of various LD photodetectors with different plasmonic structures is briefly surveyed, in order to provide a clear picture of related fabrication methods, leading to maximized plasmonic enhancement. The fundamentals of localized surface-plasmon resonance and plasmonic hot electrons are first introduced, followed by a summary of several prototypical LD photodetectors enhanced by metal nanoparticles (NPs), including noble-metal NPs, poor-metal NPs, and some plasmonic doped-semiconductor NPs. The recent achievement of the newly developed LD photodetectors propelled by plasmonic hot carriers is also highlighted. Finally, some challenges and issues that need to be resolved in this field are proposed.

to these characteristics, LD photodetectors based on atomically thin 2D materials (e.g., graphene, MoS₂, WS₂, etc.),^[3–7] 1D semiconductor nanowires (e.g., ZnO, Si, GaN, SnO₂, etc.),^[8] and 0D QDs (such as the PbS QD layer, the HgTe QD layer, and the InAs QDs in quantum wells)^[9–12] are at the forefront of photodetector research for their competitive device performance in terms of higher responsivity, high photoconductive gain, and fast response speed. While the downscaling of devices hastens the electrical signal due to the short length of the electron transport, the small volume of the LD photodetectors also suffers from low absorption of light, e.g., 2.3% for single-layer graphene.^[13]

Surface plasmon polariton (SPP) is light-excited collective oscillation of free electrons on an interface between a metal layer and a dielectric medium such as air.^[14] Under the SPP mode, the electro-

magnetic energy of light excitation is converted to the energy of an electromagnetic wave on the interface that exhibits characteristics of both the photons and the electrons. Therefore, the SPP mode can confine incident light on the surface of the metal layer below the diffraction limit, and propagate along the surface. Owing to the confinement, the SPP electromagnetic field could be enhanced by up to 10⁵.^[15] This provides a promising solution to the dilemma of LD photodetectors and therefore are widely used in thin-film plasmonic optoelectronic devices.^[16] However, excitation of SPPs on the metal layers is conditional and normally entails a special excitation setup, such as gold film-coated prism, to meet momentum conservation requirements, and therefore its use in LD photodetectors is limited. In contrast, localized surface plasmons (LSPs) can be excited by direct illumination on metal nanostructures, such as metal nanoparticles (NPs). Compared to SPP, LSP is confined on the NP surface without propagation, and its enhancement depends on NP size and geometry.^[17] Thus, well-developed fabrication methods of metal nanostructures have rendered LSPs a dominant technology for boosting the device performance of LD photodetectors in recent years.^[18]


As the photodetector materials change from bulk or thin film to the LD ones, plasmonic materials also evolve for optimized enhancement depending on the dimensions of the photodetectors of interests. Silver nanowires are deposited on a 2D MoS₂ as an SPP photodetector.^[2] Gold NPs are deposited on 1D nanowire as an LSP-enhanced photodetector.^[19] Perforated nanohole arrays are made on a gold film to directly excite

1. Introduction

The photodetector, as one of the most important optoelectronic devices, has attracted enormous research interest in the past several decades. It can absorb photons and convert them into electrical signals, which is of paramount importance for a wide range of applications, such as target detection, light vision, military surveillance, etc.^[1] In comparison with traditional bulk materials or thin films, low-dimensional (LD) semiconductor nanomaterials, including 2D nanosheets, 1D nanostructures (e.g., nanowires, nanoribbons, and nanotubes, and 0D quantum dots (QDs)), usually have the advantages of excellent volumetric light absorption and carrier transport.^[2] Owing

Dr. J.-A. Huang,^[†] Prof. L.-B. Luo
School of Electronic Science and Applied Physics
Hefei University of Technology
Hefei 230009, China
E-mail: luolb@hfut.edu.cn

Dr. J.-A. Huang
Department of Electrical and Electronic Engineering
the University of Hong Kong
Pokfulam, Hong Kong SAR, China

 The ORCID identification number(s) for the author(s) of this article can be found under <https://doi.org/10.1002/adom.201701282>.

^[†]Present address: Istituto Italiano di Tecnologia, Via Morego 30, 16163 Genova, Italy

DOI: 10.1002/adom.201701282

the SPPs for enhancing a photodetection layer of 0D quantum dots.^[20] Nonetheless, plasmonic materials are not limited to conventional noble metals. Some heavily doped semiconductors, for example, indium tin oxide (ITO) NPs or Cu_{3-x}P, can induce obvious LSPs under illumination of near-infrared light, and therefore they are used to enhance near-infrared photodetectors.^[21] Although most plasmonic devices are enhanced by the electric field of the SPP and LSP modes, other mechanisms, such as leaky-mode resonances and plasmonic hot-electron injection, are found to be responsible for the high performance of nanocone photodetectors^[22] and of Schottky-junction-based photodetectors.^[23] In fact, both the photodetector materials and the plasmonic materials can be low dimensional. The plasmonic materials are fabricated according to the dimensions of the photodetector materials to maximize the photodetection enhancement. In some cases, the enhancement effects of the LD plasmonic photodetectors could be multiple and can coexist.

In this review, we will summarize recent progress on LD plasmonic photodetectors made in the past few years, and categorize them by the plasmonics technologies used for enhancement, giving a clear picture of related fabrication methods, as well as of the underlying enhancement mechanism. We first introduce the enhancement mechanisms of an LSP resonance (LSPR) and plasmonic hot electrons. In Section 3, we describe the photodetectors enhanced by metal NPs, including noble-metal NPs, poor-metal NPs, metal NP arrays, and other forms of metal nanostructures. Plasmonic doped-semiconductor NPs are presented in Section 4. In Section 5, we elucidate LD photodetectors enhanced by the state-of-the-art plasmonic hot carriers, including metal-insulator-metal, metal-semiconductor, and metal-nanomaterial photodetectors. Finally, we present conclusions and an outlook of future opportunities and challenges in the field of LD plasmonic photodetectors.

2. Fundamentals

Generally, there are two detection mechanisms for LD plasmonic photodetectors. The first is the plasmonic NPs at the resonant wavelength of an LSPR that act like optical antennas to trap light with energy larger than the semiconductor bandgap. The enhanced local electric field due to an LSPR on the surface of the plasmonic NPs can excite the semiconductor to generate more electron-hole pairs for enhanced photocurrents. Another detection mechanism is the enhanced internal photoemission of hot carriers at a Schottky junction formed between the metal NPs and the semiconductors due to the enhanced absorption of the metal NPs at an LSPR.^[16]

2.1. LSPR of Metal NPs

Since the size of the metal NP of interest in this review is generally smaller than the incident wavelength, the optical response of the NP can be approximated by a quasistatic dipole with the following dipole moment^[24]



Jian-An Huang received his B.Sc. in Applied Chemistry from the University of Science and Technology of China in 2004. He joined the group of Prof. Shuit-Tong Lee in the City University of Hong Kong in 2009 and obtained his Ph.D. in Materials Science and Engineering in 2013. His Ph.D. research was to develop a reproducible surface-

enhanced Raman spectroscopy (SERS) substrate based on silicon nanopillar array for biomolecular detection and microfluidic SERS chips. During 2013–2016, he worked as a Research Associate at the University of Hong Kong on scanning near-field optical microscopy/spectroscopy studies of GaN microLED. After short visit at the Hefei University of Technology, he then obtained a position at the Italian Institute of Technology at Genova, Italy, where he is now a postdoc researcher. His research interests include surface-enhanced Raman spectroscopy, scanning near-field optical microscopy, and plasmonic semiconductor nanostructures.



Lin-Bao Luo received M.Sc. in inorganic chemistry at the Department of Chemistry, University of Science and Technology of China under the supervision of Prof. Shu-Hong Yu in 2006, and Ph.D. Degree from the Department of Physics and Materials Sciences, City University of Hong Kong under the guidance of

Prof. Shuit-Tong Lee in 2009. After spending one and half years at the same group as a research associate, he joined the School of Electronic Sciences and Applied Physics, Hefei University of Technology, where he is now a full professor of applied physics. He has published more than 100 peer refereed journals articles with a total citation of 3000 and an *h*-index of 28. His research interest mainly focuses on controlled fabrication of low-dimensional semiconductor nanostructures for high-performance optoelectronic and electronic device applications including photodetectors, photovoltaic devices, and nonvolatile memory devices.

$$P = 4\pi\epsilon_m a^3 \frac{\epsilon_p - \epsilon_m}{\epsilon_p + 2\epsilon_m} E_0 \quad (1)$$

where ϵ_p and ϵ_m are the dielectric functions of the NP and the medium embedding the NP, respectively. The NP cross-sections for scattering, C_{sca} ; absorption, C_{abs} ; and extinction, C_{ext} ; can be deduced from the field of the dipole moment as

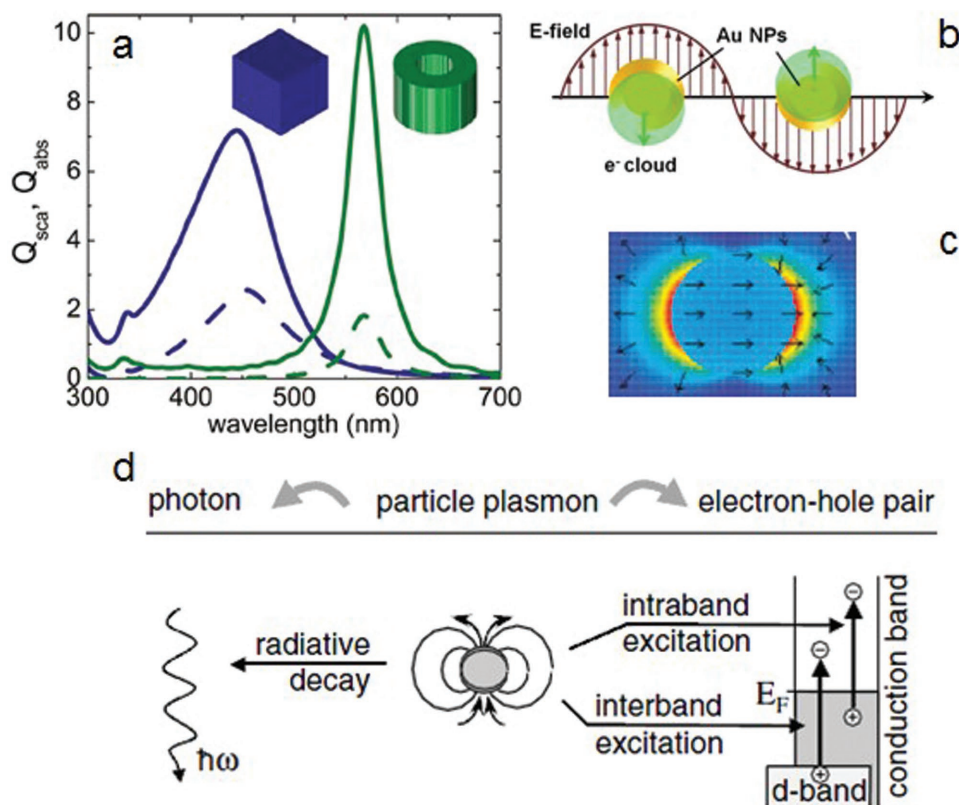


Figure 1. a) Calculated absorption (solid lines) and scattering (dashed lines) efficiencies ($Q = C/\sigma$) for a cube- (blue) and a ring- (green) shaped silver NP. The particles have similar dimensions; both the side of the cube and the diameter of the ring are 50 nm. b) Schematic of the LSPR. c) Simulated electric field intensity of a metal NP under LSPR. d) Schematic of radiative (left) and nonradiative (right) decay of particle plasmons in a metal NP. The nonradiative decay occurs via excitation of electron-hole pairs either within the conduction band (interband excitation) or between the d band and the conduction band (intraband excitation). (a–c) Reprinted with permission.^[25] Copyright 2011, American Chemical Society. (d) Reprinted with permission.^[26] Copyright 2002, American Physical Society.

$$C_{\text{sca}} = \sigma \frac{8}{3} (ka)^4 \left| \frac{\epsilon_p - \epsilon_m}{\epsilon_p + 2\epsilon_m} \right|^2, \quad C_{\text{abs}} = \sigma 4(ka) \text{Im} \left[\frac{\epsilon_p - \epsilon_m}{\epsilon_p + 2\epsilon_m} \right], \quad (2)$$

$$C_{\text{ext}} = C_{\text{sca}} + C_{\text{abs}}$$

where k is the wave vector, a is the NP diameter, and $\sigma = \pi a^2$ is the NP geometric cross-section. Since $C_{\text{sca}} \propto a^4$ and $C_{\text{abs}} \propto a$, light scattering dominates the optical response of large NPs and absorption dominates that of small NPs. From these formulas, resonant enhancement at both C_{sca} and C_{abs} can occur when $\epsilon_p = -2\epsilon_m$ (the Fröhlich condition) is satisfied. Both the scattering and absorption cross-sections are a few times larger than the geometric cross-section of NP (σ), leading to enhanced scattering and absorption of the NP as shown in Figure 1a.

In the case of metal NPs (MNPs), the Fröhlich condition corresponds to the LSPR, that is, the coherent collective oscillation of the free electrons within the metal NP.^[25] Since the size of the MNPs is smaller than the wavelength of the incident light and optical penetration depth, all the free electrons in the MNP can be collectively excited. The collective oscillation of the electrons can be regarded as a displacement of the center of mass of all the electrons in the MNP against the positively charged matrix of the atomic cores (Figure 1b).^[14] This collective charge oscillation leads to a resonant enhancement of the local field on the surface of the MNP (Figure 1c), which is useful for numerous

optoelectronic device applications, including plasmonic photo-detectors, solar cells, and light emitting diodes (LEDs).^[25] The resonance wavelength and the linewidth of the LSPR are determined by the dielectric properties of the MNP (ϵ_p) and the surrounding medium (ϵ_m), as well as by the MNP size and shape.

2.2. LSPR of Doped-Semiconductor NPs

The enhanced local field due to the MNP LSPR exists only for a short time: $T_2 = 2\hbar/\Gamma$, where Γ is the LSPR linewidth.^[26,27] After T_2 , the coherent collective oscillation of the free electrons and the associated enhanced local field will lose phase coherence with respect to the excitation light, and decay to either the excitation of electron-hole pairs in the MNP or to the photon emission to the far field (Figure 1d). Thus, T_2 is called the dephasing time and is on the order of $\approx 4\text{--}20$ fs.^[27] In applications relying on the enhanced local field of the MNP, both the radiative decay and the intraband/interband excitation of the electron-hole pairs are viewed as losses.

For the case of noble metals such as Au and Ag, the band structure includes sp and d bands.^[28] The sp bands crossing the Fermi level are occupied by the free electrons. Transitions within the sp bands are intraband excitations that can be described by the Drude model. Optical transitions between the filled d band

and the empty states of the sp band are interband excitations. The NP dielectric function ϵ_p characterizing the intraband transitions of the MNP free electrons can be described using the Drude model as^[24,29]

$$\epsilon_p(\omega) = \epsilon' + i\epsilon'' = \epsilon_b - \frac{\omega_p^2}{\omega^2 + \gamma^2} + i \frac{\omega_p^2 \gamma}{(\omega^2 + \gamma^2)\omega} \quad (3)$$

where $\gamma = v_F/l$ is the bulk damping rate that is related to the mean free path l of the electrons and the Fermi velocity v_F .^[24] The plasma frequency is given by $\omega_p = (ne^2/\epsilon_0 m_e)^{1/2}$, where n is the electron density, ϵ_0 is the vacuum permittivity, and m_e is the effective mass of the electrons.^[24,27] For the interband transition loss, the onset of the interband transition is at ≈ 2.4 eV for Au and 3.9 eV for Ag. For small MNPs with diameters less than the mean free path of the free electrons, loss can be grain-boundary scattering of the electrons. Together with the scattering/Ohmic losses that would lower the lifetime of the enhanced local field, MNP suffers from many drawbacks in integration with plasmonic photodetectors, such as ease of oxidation, especially for Ag NPs, incompatibility with the complementary metal–oxide–semiconductor manufacturing process, and nontunable LSPR frequency.^[29] These drawbacks can be partially overcome by introducing the LSPR of nonmetal nanocrystals.

Nonmetal nanocrystals are doped colloidal semiconductor and metal-oxide nanocrystals whose sizes are on the order of a few tens of nanometers. They can exhibit an LSPR because they have a high concentration of free carriers to support the coherent collective charge oscillation under light excitation. Therefore, in the optical spectrum, their optical response can be elucidated by the quasistatic dipole oscillators as Equation (1) and the Drude model in Equation (3). The Fröhlich condition ($\epsilon_p = -2\epsilon_m$) is also applicable to estimate the LSPR of the nonmetal nanocrystals.

The most prominent advantage of the nonmetal nanocrystals lies in their free-carrier concentration, controllable by doping, which can tune their LSPR frequency and suppress losses. According to the Drude model in Equation (3), the plasma frequency ω_p and the bulk damping rate γ are^[24,29]

$$\omega_p = \sqrt{\frac{ne^2}{\epsilon_0 m^*}}, \quad \gamma = \frac{e}{\mu m^*} \quad (4)$$

where n is the free-carrier concentration, m^* is the effective mass of the free carrier, and μ is the carrier mobility. The LSPR frequency (ω_{LSPR}) is determined by the free-carrier concentration according to the Fröhlich condition ($\epsilon' = -2\epsilon_m$) as

$$\omega_{\text{LSPR}} = \sqrt{\frac{ne^2}{\epsilon_0 m^* (\epsilon_\infty + 2\epsilon_m)} - \gamma^2} \quad (5)$$

This equation is also used to deduce the carrier concentration by the measured LSPR wavelength. To make a semiconductor behave like a metal, the semiconductor carrier concentration must be high enough that the real part of the semiconductor dielectric function, ϵ' , becomes negative. Therefore, the minimum carrier concentration for a metal-like semiconductor can be determined by a crossover frequency, ω_c , at which $\epsilon' = 0$, as^[24,29]

$$n_{\text{min}} = \frac{\epsilon_\infty \epsilon_0 m^*}{e^2} (\omega_c^2 + \gamma^2) \quad (6)$$

As an example, the minimum carrier concentration of n-Si to achieve $\epsilon' = -1$ at a telecommunication wavelength of 1550 nm is estimated as $1.6 \times 10^{21} \text{ cm}^{-3}$.^[29] Compared with the free-electron concentration ($\approx 10^{23} \text{ cm}^{-3}$) in metal, the carrier concentration of nonmetal nanocrystals is two orders less in magnitude, which contributes to the much lower loss characterized by $\epsilon'' \propto \omega_p^2 \propto n$. The relatively low carrier concentration of the nonmetal nanocrystals limits the LSPR to the near-infrared spectrum and beyond, which is generally less than their optical bandgap and exempted from interband loss. Another way to reduce the loss is to select the semiconductor nanocrystals with high mobility and large effective mass because of the damping rate $\gamma = e/(\mu m^*)$.

2.3. Plasmonic Hot Electrons

Together with the above efforts devoted to suppressing the Ohmic loss, the excitation of electron–hole pairs by MNP LSPR dephasing has been explored to increase the internal photoemission (IPE) of hot carriers through Schottky contact formed between the MNP and the semiconductors. The energetic electron–hole pairs have different levels in energy depending on the intraband or interband excitations. They then will be equilibrated by electron–electron scattering, for which it takes 100 fs to achieve hot-electron distribution, as shown in **Figure 2a**.^[27] The hot-electron distribution actually removes the memory of how the electron–hole pairs are excited. Then, the hot-electron distribution will relax by electron–phonon scattering on a timescale of 1 ps, and will finally couple to heat transferred to the surrounding environment in more than 10 ps.

As shown in **Figure 2b**,^[23] IPE consists of three steps: the generation of hot carriers in the MNPs by optical absorption, the transport of the hot carriers to the Schottky junction, and the emission of the hot carriers over the Schottky barrier into the semiconductor, where they are collected as photocurrent under reverse bias.^[16] The excitation light should have an energy larger than the Schottky barrier energy (Φ_B). The advantage of IPE is the sub-bandgap detection ($\Phi_B < h\nu < E_g$) that enables photodetection of optical energy below the semiconductor bandgap.

The excitation of the LSPR in MNPs will induce enhanced optical absorption, which is advantageous in the generation of hot electrons. The energy distribution of hot carriers is found to be proportional to the field-enhancement factor inside the MNPs.^[30] For example, an Au ellipsoid exhibits efficient generation of hot electrons because the internal field enhancement of an Au ellipsoid is the largest among Au slabs, Au nanocubes, and Au nanospheres.^[27] During transport, however, the energy of the hot carriers in the MNPs can be coupled to the heat via electron–phonon scattering and grain boundary scattering.^[27] Therefore, the mean free path of the hot electrons of the MNPs, $l = v_F/\gamma$, where v_F is the Fermi velocity, should be larger than the MNP size to ensure efficient transport of the hot electrons to the Schottky junction. As an example, in Au NPs, hot electrons

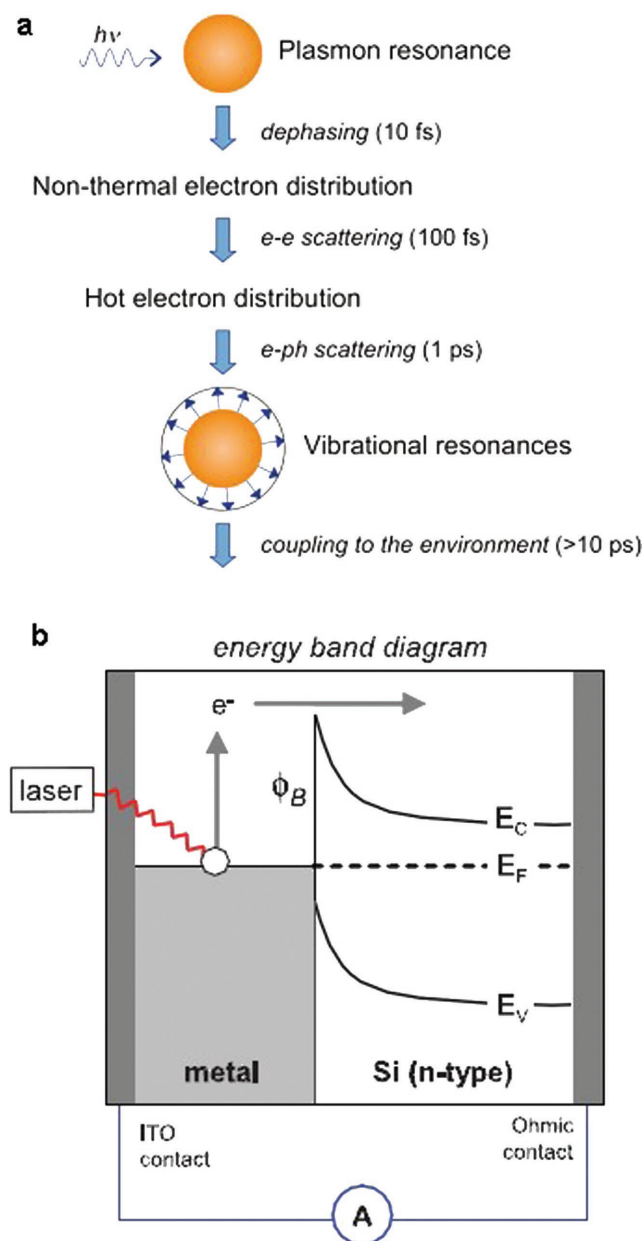


Figure 2. a) Temporal evolution of LSP in a metal nanoparticle. b) Energy-band diagram for plasmonically driven internal photoemission over a nanoantenna-semiconductor Schottky barrier (Φ_B). (a) Reprinted with permission.^[27] Copyright 2011, American Association for the Advancement of Science. (b) Reprinted with permission.^[23] Copyright 2011, American Chemical Society.

under excitation energy of 1–2 eV have a mean free path of 17–50 nm.^[28] Thus, Au NPs with a size less than 50 nm will exhibit the most efficient hot-electron transport. Furthermore, the hot electrons transported to the metal-semiconductor interface might be reflected back due to the momentum mismatch. This case is less possible at a rough MNP-semiconductor interface.^[28] The injection rate of the hot electrons over the MNP-semiconductor interface can be approximated by the Fowler equation^[23]

$$\eta_i \approx C_F \frac{(h\nu - q\Phi_B)^2}{h\nu} \quad (7)$$

where C_F is a coefficient subject to device-specific details. By using this equation, the barrier height Φ_B can be obtained by fitting the measurement data.

3. LD Plasmonic Photodetectors Based on Metal NPs

3.1. LD Plasmonic Photodetectors Based on Random-Metal NPs

The easiest way to coat MNPs onto LD photodetectors is to deposit a metal film and then anneal it in inert gas, which leads to randomly distributed MNPs. The NP diameters and the LSPR wavelength could be tuned by controlling the film thickness. By matching the LSPR to the absorption band of the LD photodetectors, the trapped and enhanced electric fields on the NP surfaces could excite the photodetectors for plasmon-enhanced photodetection. This annealing method has been widely used to enhance 1D and 2D photodetectors. Luo et al. annealed a gold film on single-crystal CdTe nanowires at 350 °C for 40 min in Ar gas and obtained Au NPs with an LSPR at ≈ 510 nm (Figure 3a,b).^[19] As indicated in Figure 3c, once the device was modified with Au NPs, the dark current was reduced while the photocurrent was increased, leading to an obvious increase in switch ratio and responsivity. Moreover, the response speed of the 1D plasmonic photodetector was accelerated from 6.12 to 1.92 s (Figure 3d). A sensitive ultraviolet photodetector with similar geometry was fabricated by annealing the Au film on a ZnO nanorod array at 450 °C under vacuum.^[31] It was observed that, after surface modification, the rejection ratio increased dramatically from 214 to 6180. In addition, the quantum efficiency was enhanced 11.57-fold.

In the case of 2D materials, graphene is a representative material that exhibits high carrier mobility, transparency, and mechanical flexibility. The optoelectronic applications based on graphene have attracted tremendous interest, including light-emitting devices and photodetectors.^[4,32] However, the performances of graphene-based photodetectors have always been limited by low absorption, difficulty of photoelectron extraction, and photocurrent counterbalance between the contacts.^[33] Plasmonic nanoparticles exhibiting strong absorption cross-sections thus have been widely applied to graphene photodetectors to improve the photoresponsivity.^[5,34–39] As the first demonstration, Liu et al. obtained gold NPs by annealing gold film deposited on silica wafer, and then used a poly(methyl methacrylate) (PMMA) layer to transfer the NPs onto a back-gated graphene phototransistor.^[34] The carrier mobility of the Au NP-integrated graphene device was in the range 1000–2000 $\text{cm}^2 \text{V}^{-1} \text{s}^{-1}$. The Au NPs exhibited LSPRs and photocurrent enhancement at wavelengths between 500 and 700 nm, depending on the gold-film thickness, which ranged from 4 to 12 nm. In particular, the Au NPs of 110 nm diameter obtained by annealing 12 nm thick gold film led to photocurrent enhancement as high as 15-fold at 520 nm illumination with a responsivity of 6.1 mA W^{-1} . Furthermore, Liu et al. demonstrated wavelength-dependent photodetection enhancement by matching the wavelength to

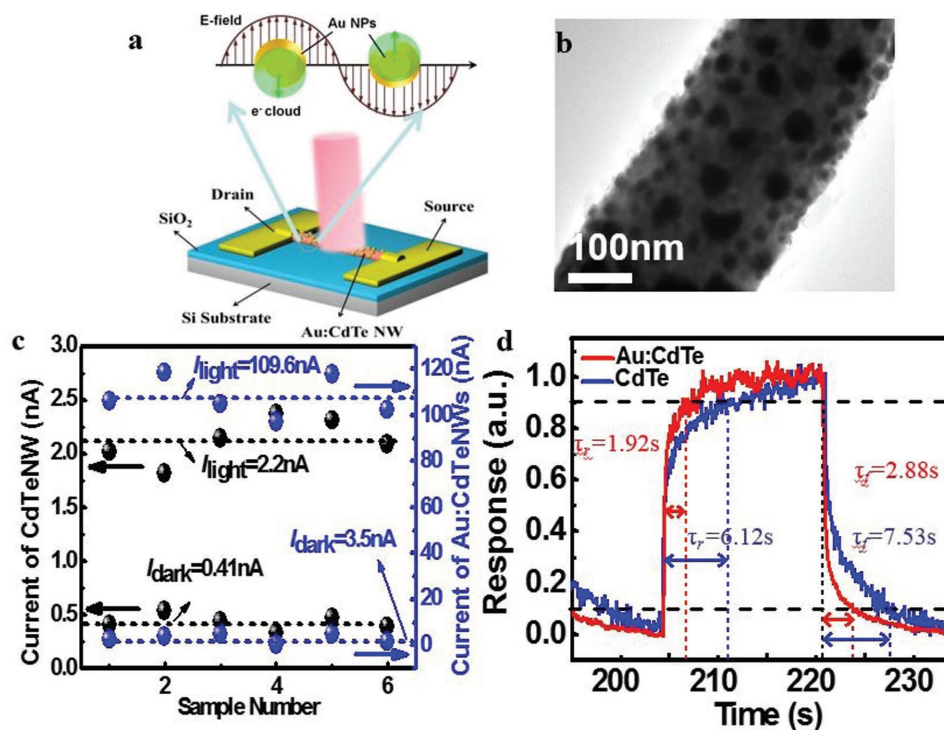


Figure 3. a) Schematic of Au NP-modified CdTe nanowire photodetector. b) Transmission electron microscopy (TEM) image of the Au NP-decorated CdTe nanowire. c) Dark current and photocurrent of six devices with and without modification. d) Single normalized cycle measured at the same incident light for estimating both the rise and fall times. Reprinted with permission.^[19] Copyright 2014, Wiley.

the LSPR of the Au NPs. Similarly, Niu et al. deposited Au NPs (\varnothing 28–68 nm) on reduced graphene oxide by annealing gold film at 350 °C, and enhanced the responsivity tenfold at a wavelength of 980 nm.^[38]

Since the dipole field of the metal NP was trapped on the metal NP surface, and annealed NPs were not wrapped by the planar 2D materials, most metal-NP–2D hybrid nanostructures had the enhanced electric field to partially excite the 2D materials. To make full use of the metal-NP electric field, Li et al. encapsulated MoS₂ on the Au NPs as a 2D plasmonic photodetector.^[40] Au NPs on a silicon substrate were first made by annealing gold film on silicon at 800 °C for 15 min. Then, the MoS₂ was grown in a tube furnace at 650 °C with the substrate facing MoO₃ such that the MoS₂ was wrapped on the Au NPs. The as-fabricated Au–MoS₂ core–shell photodetector exhibited an enhanced electric field due to the LSPR at 600 nm. As the field fully excited the MoS₂ layer, it demonstrated tenfold enhancement of responsivity (22.3 A W⁻¹) compared with planar MoS₂ detectors.

As alternatives to noble-metal NPs, poor-metal NPs have attracted an increasing amount of interest because they have large negative real and small imaginary dielectric functions, and therefore they can induce LSPRs as well. A new plasmonic red-light photodetector was fabricated by decorating a graphene–CdSe nanoribbon heterojunction with ordered copper NPs, which exhibits apparent LSPRs in the range 700–900 nm.^[41] The Cu NPs were obtained by directly sputtering the Cu metal onto the graphene/CdSe heterojunction using polystyrene spheres as a template, followed by removal

of the spheres. Optoelectronic analysis revealed that the device parameters, including switch ratio, responsivity, and detectivity, were all considerably improved. In addition, the response speed was accelerated by approximately tenfold. By using a similar fabrication method, a high-performance blue-light nanophotodetector was achieved using plasmonic indium NPs.^[42] The photocurrent was found to increase by nearly 20-fold, leading to increases in response and gain. Such optimization of device performance is due to the LSPR-induced direct electron injection from In NPs into single-layer graphene, according to a theoretical simulation based on finite-element method. In photodetection in the ultraviolet (UV) region, Lu et al. grew a ZnO nanorod array on a quartz substrate in a tube furnace, followed by sputtering deposition of aluminum NPs.^[43] The aluminum NPs with typical LSPRs at $\lambda = 380$ nm can increase the responsivity of a ZnO nanorod photodetector from 0.12 to 1.59 A W⁻¹ under a bias of 5 V.

3.2. LD Plasmonic Photodetectors Based on Colloidal Metal NPs

Despite low cost and facile fabrication, an obvious drawback of the annealed MNPs has been the wide distribution of the MNP diameters that strongly affect the LSPR wavelength and field enhancement. Random-metal NPs with wide distribution usually defy precise control over size. This is completely different from the colloidal metal NPs prepared by chemical synthesis. Not only the MNP diameters, but also the core–shell structures of the MNPs can be accurately controlled,^[44] Colloidal Au

Table 1. Performance of 1D plasmonic photodetectors using various plasmonic materials.

Plasmonic materials	Photodetection materials	Wavelength [nm]	Response time	Responsivity [$A W^{-1}$]	Detectivity [$\times 10^{11}$ Jones]	Ref.
Annealed Au NPs	CdTe nanowire	826	1.9 s	2.26×10^4	12.5	[19]
Indium tin oxide NPs	Ge nanoneedles	1550	450 ns	0.185	228	[21]
Sputtered Cu NPs	Graphene/CdSe nanoribbons	780	0.03 ms	5.5	–	[41]
Sputtered In NPs	Graphene/ZnSe nanowire	480	0.07 s	6.47×10^2	–	[42]
Sputtered Al NPs	ZnO nanowire	367	40 s	1.59	–	[43]
Colloidal Ag NPs	ZnSe nanowire	480	–	1.848×10^{-1}	9.2	[46]
Colloidal Au NPs	ZnTe nanowire	539	–	5.11×10^3	328	[47]
Colloidal hollow Au NPs	Bi_2S_3 nanowire	953	–	1.09×10^3	278	[50]
Colloidal hollow Au NPs	CdSe nanowire	729	–	4.87×10^4	750	[48]
Colloidal Au NPs	Graphene/Si nanorods	850	73 μ s	1.5	252	[49]

NPs are usually synthesized by reduction of $H AuCl_4$ solution in alcohol, while colloidal Ag NPs can be obtained by citrate reduction of $AgNO_3$ aqueous solution. By further adsorbing the colloidal MNPs on single 1D semiconductor materials in solution phase, Luo and co-workers achieved a 1D plasmonic photodetector with band-edge absorption wavelengths from the UV to near-infrared regions, including Cl-doped ZnS ($\lambda_{bandgap} = 365$ nm),^[45] ZnSe ($\lambda_{bandgap} = 480$ nm),^[46] ZnTe ($\lambda_{bandgap} = 539$ nm),^[47] CdSe ($\lambda_{bandgap} = 729$ nm),^[48] Si nanorods ($\lambda_{bandgap} = 850$ nm),^[49] and Bi_2S_3 ($\lambda_{bandgap} = 953$ nm).^[50] Details of their enhanced performance are given in Table 1. One typical example was CdSe nanoribbon enhanced by hollow gold nanoparticles

(HGNs), as shown in Figure 4.^[48] HGNs were synthesized by a sacrificial galvanic replacement process, and linked to a CdSe-nanoribbon photodetector by bis(3-mercaptopropionate) molecules for photocurrent enhancement. The HGN LSPRs can be tuned by the inner-to-outer-radius aspect ratio of the HGNs that led to photocurrent enhancement at wavelengths between 500 and 650 nm (Figure 4i,j). The device achieved a responsivity of $4870 A W^{-1}$ and a detectivity of 7.5×10^{13} Jones, which represent the most competitive values compared with other CdSe-nanoribbon-based photodetectors.

To expand the resonant absorption spectrum of a plasmonic graphene photodetector, block copolymers were used

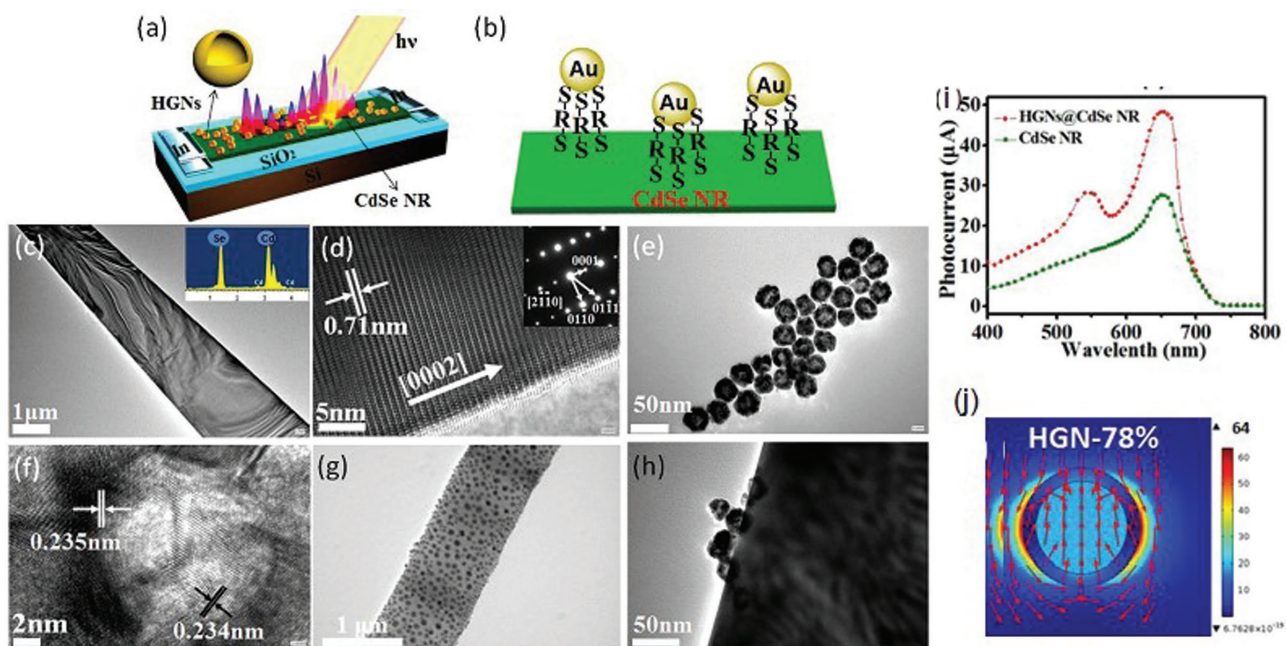


Figure 4. a) Schematic of plasmonic photodetector. b) Schematic of CdSe nanoribbon (NR) decorated with HGNs via bis(3-mercaptopropionate) molecule. c) TEM image of a single CdSe NR; inset shows the energy-dispersive X-ray spectroscopy (EDS) spectrum. d) High-resolution TEM (HRTEM) image of a CdSe nanoribbon; inset shows the corresponding selected-area electron-diffraction (SAED) patterns. e) TEM image of the HGNs. f) HRTEM image of a typical HGN. g) TEM image of a CdSe nanoribbon decorated with HGNs. h) TEM image of a CdSe nanoribbon decorated with HGNs at large magnification. i) Spectral response of CdSe nanoribbon and HGNs@CdSe nanoribbon photodetector. j) Electric field distribution at the cross-section of HGNs parallel to the polarization direction at LSP peaks. Reprinted with permission.^[48] Copyright 2014, Optical Society of America.

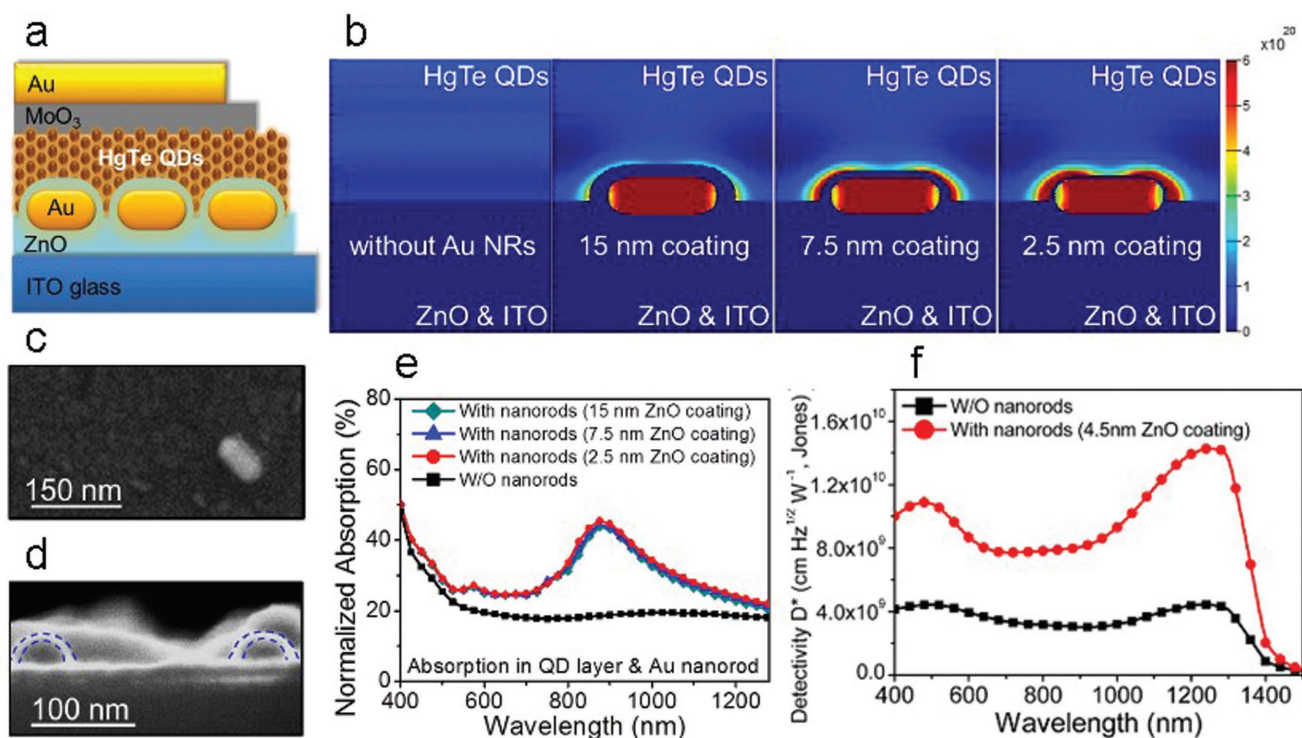


Figure 5. a) Schematic of HgTe QD/ZnO heterojunction photodiode with Au nanorods embedded within the QD layer (nanorods with ZnO coating). b) Finite-difference time-domain (FDTD) simulated 2D light-absorption distributions (cross-sections) of HgTe QD/ZnO films with and without Au nanorods at LSPR peak wavelength. Polarization of the incident wave is along the long axis of the Au nanorods. SEM images of c) top view and d) cross-section of Au nanorods with 5 min sputtering of ZnO coating. Core (Au nanorod) and shell (ZnO coating) structures are highlighted by blue dashed lines. e) Simulated total absorption spectra of the four cases shown in (b) by accounting for the absorption in the entire film. f) Detectivity spectra of the photodiodes with and without embedded nanorod structures. Reprinted with permission.^[10] Copyright 2014, American Chemical Society.

to coat colloidal Au, Ag, and Cu NPs with diameters of ≈ 10 nm on graphene.^[39] The block copolymer, polystyrene-*block*-poly(acrylic acid) (PS-*b*-PAA), could be dissolved in toluene and mixed with oleylamine-modified Au NPs. After immersion in an AgNO₃ solution, the PS-*b*-PAA formed spherical micelles consisting of a PS corona and a PAA core. The PAA chains attracted Ag⁺ ions that were reduced to Ag NPs by hydrogen plasma treatment. Moreover, quasihexagonally ordered Cu NPs were formed by mixing CuCl₂ salt with polystyrene-*block*-poly(4-vinylpyridine) (PS-*b*-P4VP) copolymers for 6 h, and then adding aqueous hydrazine. Therefore, the plasmonic graphene photodetectors enhanced by triple Au–Ag–Cu NPs were made by spin-coating the PS-*b*-PAA Au–Ag NP layers and then the PS-*b*-P4VP Cu NP layer on the graphene. The three metal NPs exhibit multiple LSPRs at 420, 520, and 610 nm, respectively, and the electron (hole) mobility of the device was 5800 (1100) cm² V⁻¹ s⁻¹. The device exhibited maximum photoresponsivities at the resonant wavelengths, demonstrating a broadband photodetection enhancement. By comparing the photocurrent of graphene photodetectors patterned by single (Au), double (Au–Ag), and triple (Au–Ag–Cu) NPs, Kim et al.^[39] concluded that the Au NPs exhibited the highest responsivity, 55 mA W⁻¹ at a wavelength of 520 nm.

Colloidal MNPs were also employed to enhance OD photodetectors that were generally based on semiconductor QD layers deposited on a substrate by large-area coating methods, such

as drop-cast, spray-on methods, and dip-coating.^[51] Together with matching the LSPR wavelength with the QD-layer absorption peak, the plasmonic enhancement strategy of QD-layer photodetectors focused on the spatial matching of the QDs to the LSPR field. Huang et al. developed a QD photodetector by using 3-aminopropyltriethoxysilane to link an 80 nm thick Ag NP monolayer on a glass substrate followed by drop-casting a CdSe/ZnS QD layer with controllable thickness.^[11] By tailoring the Ag NP LSPR at $\lambda = 400$ –600 nm, the device exhibited a (1.2–1.6)-fold responsivity enhancement for a 440 nm thick QD layer and a (2.4–3.3)-fold enhancement for a 100 nm thick QD layer. Moreover, Beck et al. synthesized PbS QDs and dip-coated them on an Au nanodot array fabricated by electron beam lithography as a QD plasmonic photodetector.^[52] At a resonant wavelength of ≈ 1100 nm, the external quantum efficiency of the device with a 100 nm thick PbS QD layer was enhanced by 45%.

These works suggest that the thin QD layer close to the plasmonic structure was better excited by the plasmonic localized field and had the largest enhancement. However, it was different for QD layers in contact with metal nanoparticles. Chen et al. investigated the performance enhancement of a QD photodetector consisting of a spray-coated, 160 nm thick HgTe QD layer in contact with Au/ZnO core/shell nanorods (Figure 5a–e).^[10] They revealed that the highest enhancement of 240% was demonstrated by Au nanorods covered by a 4.5 nm

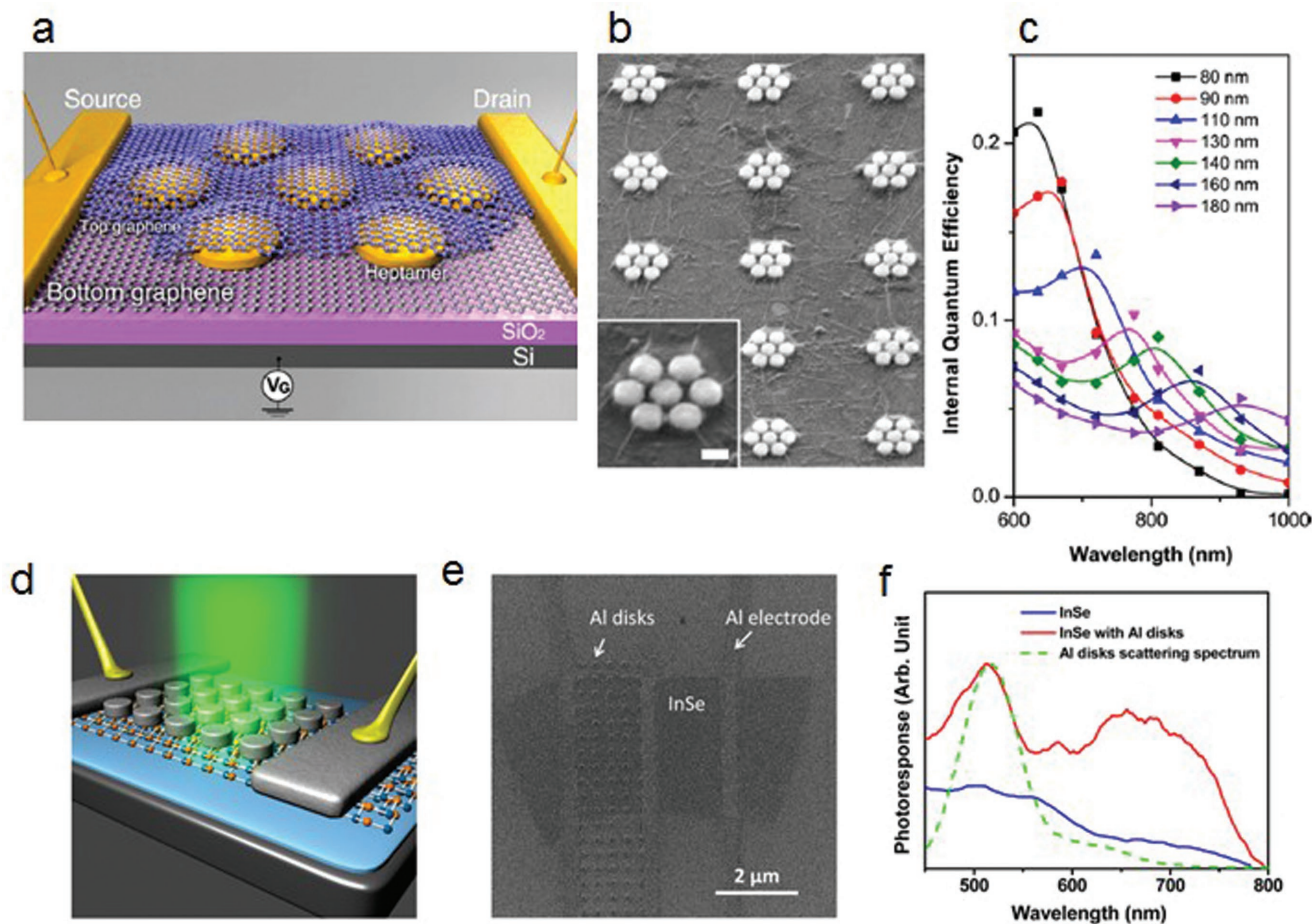


Figure 6. a) Schematic and b) SEM image of the graphene–Au aptamer–graphene sandwich photodetector. Inset is the magnified SEM image and the scale bar is 100 nm. c) Shift of enhancement wavelength of the sandwiched graphene–Au aptamer–graphene photodetector with different diameters of the Au nanodisks. d) Schematic, e) SEM image, and f) photocurrent performance of the Al nanodisk–InSe avalanche photodetector. (a–c) Reprinted with permission.^[37] Copyright 2012, American Chemical Society. (d–f) Reprinted with permission.^[54] Copyright 2015, American Chemical Society.

thick ZnO shell (Figure 5f). The photoresponse performance of bare Au nanorods in contact with the QD layer was even worse than that of a reference sample without nanorods, probably owing to exciton quenching and trap-assisted charge recombination on the Au nanorod surface.

3.3. LD Plasmonic Photodetectors Based on Metal-NP Array

An advantage of a metal-NP array lies in the convenience by which it intensifies the electric fields of LSPs between the metal NPs in the array. An engineered small gap (<10 nm) between the adjacent metal NPs exhibited LSP coupling that led to a very large gap field.^[17] Owing to the array geometry, metal-NP arrays are usually applied to enhance 2D photodetectors.^[7,53] To extend the enhanced photodetection spectrum of graphene from the visible to near-infrared bands, Fang et al. sandwiched an array of gold aptamer antennas between two graphene monolayers to form a graphene–antenna photodetector.^[37] As shown in Figure 6a,b, the gold aptamer consisted of seven 130 nm diameter Au nanodisks with an interdisk distance of 15 nm, the sizes of which could be adjusted to tune the

LSPR at wavelengths from 650 to 950 nm. Because the LSPR of the gold aptamer exhibited pronounced absorption and suppressed radiative decay, the device photocurrent was enhanced by 800% through an enormous amount of hot-carrier generation, as well as by photoelectron excitation due to the strong local electric field (Figure 6c). The sandwiched photodetector achieved an internal quantum efficiency of up to 20% in the visible and near-infrared spectrums, and a responsivity of 13 mA W⁻¹.

Together with graphene, other atomically thin 2D materials for photodetector application include transition-metal dichalcogenides, e.g., MoS₂,^[6,55] and III–VI layered semiconductors, e.g., InSe.^[56] These 2D materials have bandgaps that can increase the photon absorption and electron–hole generation, but their light absorption is still low due to their limited thickness, which can be improved by plasmonic nanoparticles.^[54,57,58] For instance, to optimize the quantum efficiency and dark current, Lei et al. demonstrated an enhanced avalanche effect by implanting plasmonic 150 nm diameter aluminum nanodisks on an InSe avalanche photodetector, as shown in Figure 6d,e.^[54] Under a bias between 12 and 50 V applied to the large Schottky barrier between the InSe monolayer and the aluminum electrodes,

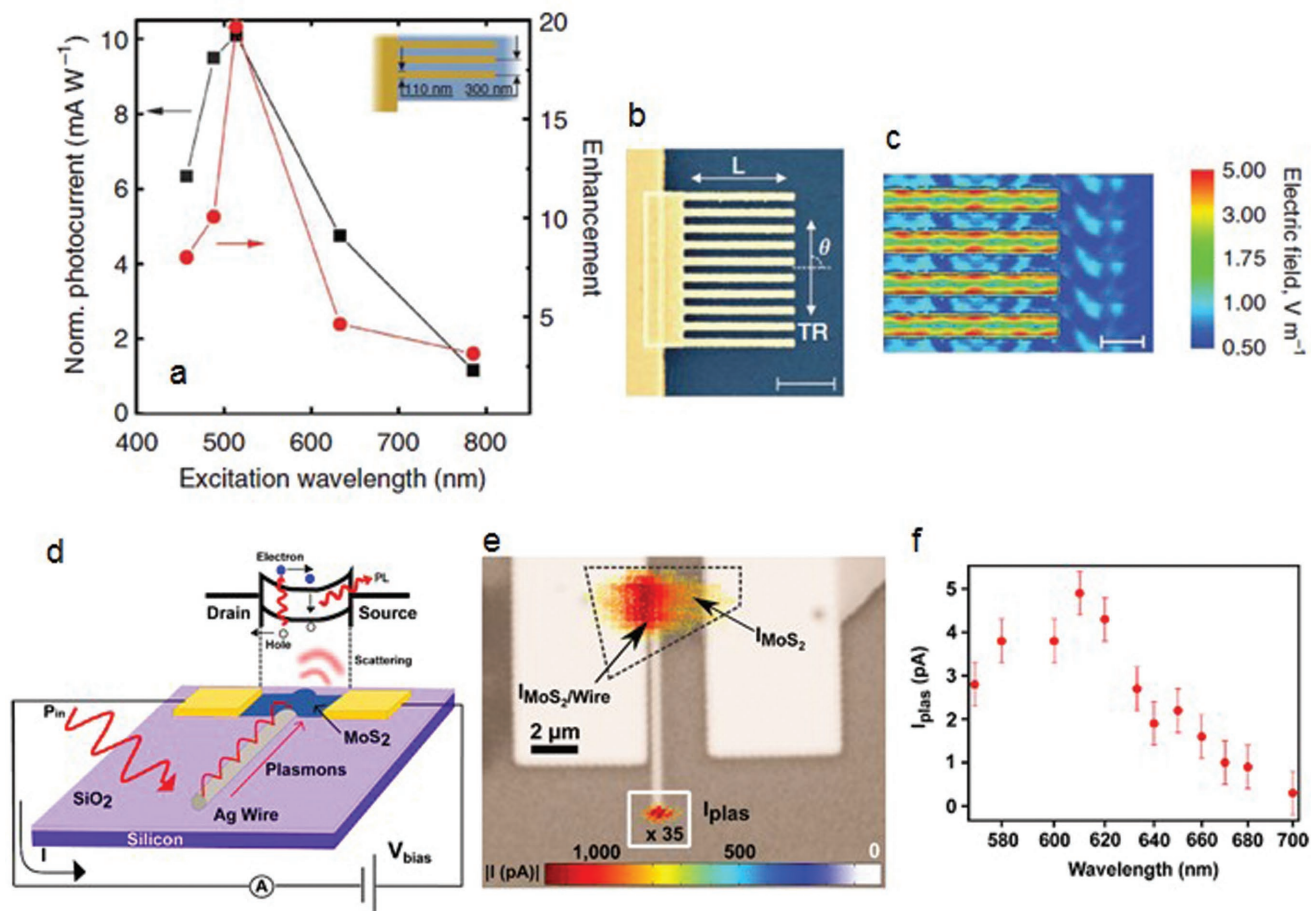


Figure 7. a) Photocurrent performance and enhancement. b) SEM image and c) FDTD simulation of the electric field of the Au nanograting–graphene photodetector. d) Schematic, e) SEM image, and f) photocurrent performance of the Ag nanowire–MoS₂ plasmonic photodetector. (a–c) Reprinted with permission.^[35] Copyright 2011, Nature Publishing Group. (d–f) Reprinted with permission.^[57] Copyright 2015, American Chemical Society.

photoelectrons required for the carrier multiplication were generated by the enhanced local field and hot-electron decay of the plasmonic aluminum nanodisks at the resonant wavelength. The device achieved an external quantum efficiency of 344%, a dark current less than tens of picoamperes, and a response time of 60 μs at a resonant wavelength of 510 nm under a bias of 30 V, as in Figure 6f. Miao et al. compared the performance of random 4 nm thick Au NPs and an ordered 160 nm wide Au nanosquare array deposited on a few-layer-thick MoS₂ phototransistor.^[58] The former exhibited twofold photocurrent enhancement at a resonant wavelength of 700 nm and the latter achieved threefold photocurrent enhancement at a resonant wavelength of 600 nm, due to the plasmonic electric field for converting incident light to electrons.

3.4. LD Plasmonic Photodetectors Based on Other Metal NPs

In addition, other different metal nanostructures were developed to excite SPPs under direct illumination and to demonstrate proof-of-concept devices. Echtermeyer et al. explored a plasmonic electrode of a graphene photodetector to overcome

the photocurrent offset between the electrodes in a condition of uniform flood illumination.^[35] Having compared the plasmonic enhancement of several metal nanostructures, the authors found that nanogratings exhibited the best performance. As shown in Figure 7a,b, a device comprising one nanograting electrode of 110 nm strip width and 300 nm pitch deposited on graphene exhibited a carrier mobility of 5000 cm² V⁻¹ s⁻¹ at room temperature. When the incident polarization was parallel to the nanostripes, the nanograting acquired an LSPR at ≈520 nm that coupled the incident light to an enhanced electric field near the nanograting electrode, and led to increased positive photocurrent (Figure 7c). The enhancement was up to 20-fold, and the corresponding responsivity was increased to 10 mA W⁻¹ at a wavelength of 520 nm.

To achieve a sub-diffraction nanoscale photodetector, Goodfellow et al. tried to integrate an Ag nanowire into a MoS₂ photodetector for near-field detection of surface plasmons, as shown in Figure 7d,e.^[57] The Ag nanowire acted as a waveguide of the surface plasmons that were excited by light irradiation (λ = 635 nm) at one free end of the wire, that propagated along the wire to the other end covered by the MoS₂, and that were finally detected by the MoS₂ photodetector. Different from the

graphene photodetectors, such a device can allow SPs to excite the electron–hole pairs across the bandgap of the MoS₂, which helps achieve a plasmon-to-charge conversion efficiency of 50% and a responsivity of $\approx 255 \text{ mA W}^{-1}$ at $\lambda = 635 \text{ nm}$ under a bias of 5 mW, as shown in Figure 7f. Moreover, there are other device configurations of single nanowire plasmonic detectors to optimize the performance. By placing a Ge nanowire photodetector into a plasmonic Ag nanoslit, a 3.7-fold photocurrent enhancement by the strong localized electric field in the slit was achieved.^[59] When Ag nanofilm was coated on a perylene nanowire, the resultant perylene@Ag core–shell nanowire photodetector achieved a 16-fold enhancement of the photocurrent compared to a perylene nanowire photodetector.^[60] Moreover, the decoration of plasmonic nanostructure is also beneficial for photoconductive gain and response speed. Wang et al. embedded Au NPs in the core of a silica nanowire photodetector that exhibited an LSPR at $\lambda = 500 \text{ nm}$ and achieved high photoconductive gain with fast rise (141 μs) and decay (298 μs) times.^[61]

Semiconductor nanorod array photodetectors that can be fabricated on large areas are more suitable for practical devices compared to single-nanowire ones. Thus, plasmonic nanostructures with large-area enhancement were needed for the nanorod photodetectors.^[31,43,62–64] Senanayake et al. grew 200 nm diameter p-type InGaAs nanorod arrays on an n⁺-GaAs wafer, planarized the array by using benzocyclobutene, exposed the nanorods by plasma etching, and deposited an Au film on the nanorod array at a tilted angle.^[64] The resultant elongated Au nanohole array acts as 2D plasmonic crystals that exhibit an enhanced electric field in the nanoholes where the InGaAs nanorods were located, and absorbed the energy. The photodetector exhibited a responsivity of 0.28 A W^{-1} at $\lambda = 1100 \text{ nm}$ under a reverse bias of -5 V . In another work, the same authors employed similar strategy to enhance an n-GaAs/p-GaAs core/shell nanorod array avalanche photodetector using elongated Au nanoholes.^[63] The enhanced electric field was overlapped with the core/shell p–n junction that acted as a multiplication region, so that an avalanche gain of ≈ 216 at $\lambda = 700 \text{ nm}$ under a bias of -12 V was achieved.

Metal nanohole arrays could excite SPPs by direct illumination due to light coupling by the Bragg scattering effect, and are frequently used to enhance 0D dots-in-a-well (DWELL) photodetectors.^[65] The DWELL photodetector was fabricated by growing, for example, InAs QDs in quantum wells consisting of InGaAs/AlGaAs pairs, providing controllable absorption wavelength and low dark current. The inter-sub-band transitions of the conduction bands of the DWELL system allow infrared absorption at $\lambda = 3\text{--}9 \mu\text{m}$, and dual absorption bands are possible due to bound-to-bound and bound-to-continuum transitions.^[9] As a typical example, Chang et al. fabricated a 50 nm thick membrane of an Au nanohole array on a top mesa of a DWELL infrared photodetector by optical lithography and metal lift-off, as shown in Figure 8a,b,f.^[20] The DWELL photodetector had two absorption bands at $\lambda = 5$ and $9 \mu\text{m}$ (Figure 8d), and the period of $1.2 \mu\text{m}$ diameter Au nanoholes could be adjusted to $3.2 \mu\text{m}$ to acquire an SPR at $\lambda = 8.8 \mu\text{m}$, achieving 65% photoresponse enhancement under a bias of -5 V . Since the nanohole period determined the SPR coupling and the nanohole diameter controlled the transmission, the authors then fixed

the period as $3.2 \mu\text{m}$, and changed the hole diameter to $1.6 \mu\text{m}$ to obtain a 130% enhancement (Figure 8g). The decay length of the enhanced field of the nanohole at the SPR was $0.8 \mu\text{m}$ (Figure 8c). By modeling the spatial matching between the electric field and the QD layer, it was concluded that a tenfold enhancement was possible for a $0.5 \mu\text{m}$ thick QD layer overlapping with the Au nanohole array.

Other work on plasmonic DWELL photodetectors was focused on the engineering of the metal nanohole array. Sheno et al. used a square-shaped Au nanohole array with a tunable SPR between 5.5 and $7.2 \mu\text{m}$, and achieved a fivefold enhancement in detectivity.^[9] By sandwiching the DWELL system between an Au membrane with a nanohole array and an Au film,^[65] a sensitive photodetector with obvious photocurrent enhancement due to an SPR as well as Fabry–Pérot mode was achieved. Furthermore, Lee et al. integrated an Au nanohole-enhanced DWELL system with a read-out circuit as a monolithic plasmonic QD infrared camera.^[66] This as-fabricated device exhibited infrared images with 160% enhancement in signal-to-noise voltage at $\lambda = 6.1 \mu\text{m}$.

4. LD Plasmonic Photodetectors Based on Doped-Semiconductor NPs

Compared to plasmonic metal nanoparticles, the nonmetal plasmonic photodetectors, such as plasmonic ITO, have the advantages of low loss and tunable LSPR. By tailoring the carrier density via impurity doping, the semiconductor plasmonic materials can induce LSPR in the infrared region, where conventional metal nanoparticles such as Au NPs exhibited no resonance. Owing to this, plasmonic doped-semiconductor NPs can play a role in photodetection at biological (650–1350 nm) and communication (1260–1675 nm) bands.^[24,29,67]

Lu et al. successfully covered a germanium nanoneedle (GeNN) array with single-layered graphene (SLG) as a Schottky-junction photodetector on which heavily Sn-doped ITO NPs were decorated for performance optimization.^[21] The heavily doped ITO NPs were synthesized by a reflux method in oleylamine, in which the doping level of Sn was controlled by tuning the In/Sn atomic ratios. Then, the ITO NPs were modified onto the SLG by spin-coating the ITO NP suspension. LSPRs ranging from 1580 to 1760 nm could be readily tailored by increasing the Sn doping level from 5% to 30%. Once the graphene–GeNN device was modified by a 10% Sn-doped ITO NP with a resonant wavelength at 1550 nm , both the responsivity and the detectivity were considerably increased to 185 mA W^{-1} and $2.28 \times 10^{13} \text{ Jones}$ at $\lambda = 1550 \text{ nm}$, respectively. Similar to the heavily doped ITO NPs, Cu_{3–x}P NPs also have high carrier concentrations due to the defects, and thus can induce the LSPR in the infrared region. Sun et al. reported the synthesis of Cu_{3–x}P nanocrystal solution by a standard air-free Schlenk line method in a three-neck flask, and then spin-cast the nanocrystals on a graphene photodetector after annealing at $200 \text{ }^\circ\text{C}$ for 2 h in vacuum.^[68] The as-made flexible plasmonic photodetector exhibited broadband photoresponse from 400 to 1550 nm , achieving a responsivity of $1.59 \times 10^5 \text{ A W}^{-1}$ at a wavelength of 405 nm and a responsivity of 9.34 A W^{-1} at 1550 nm .

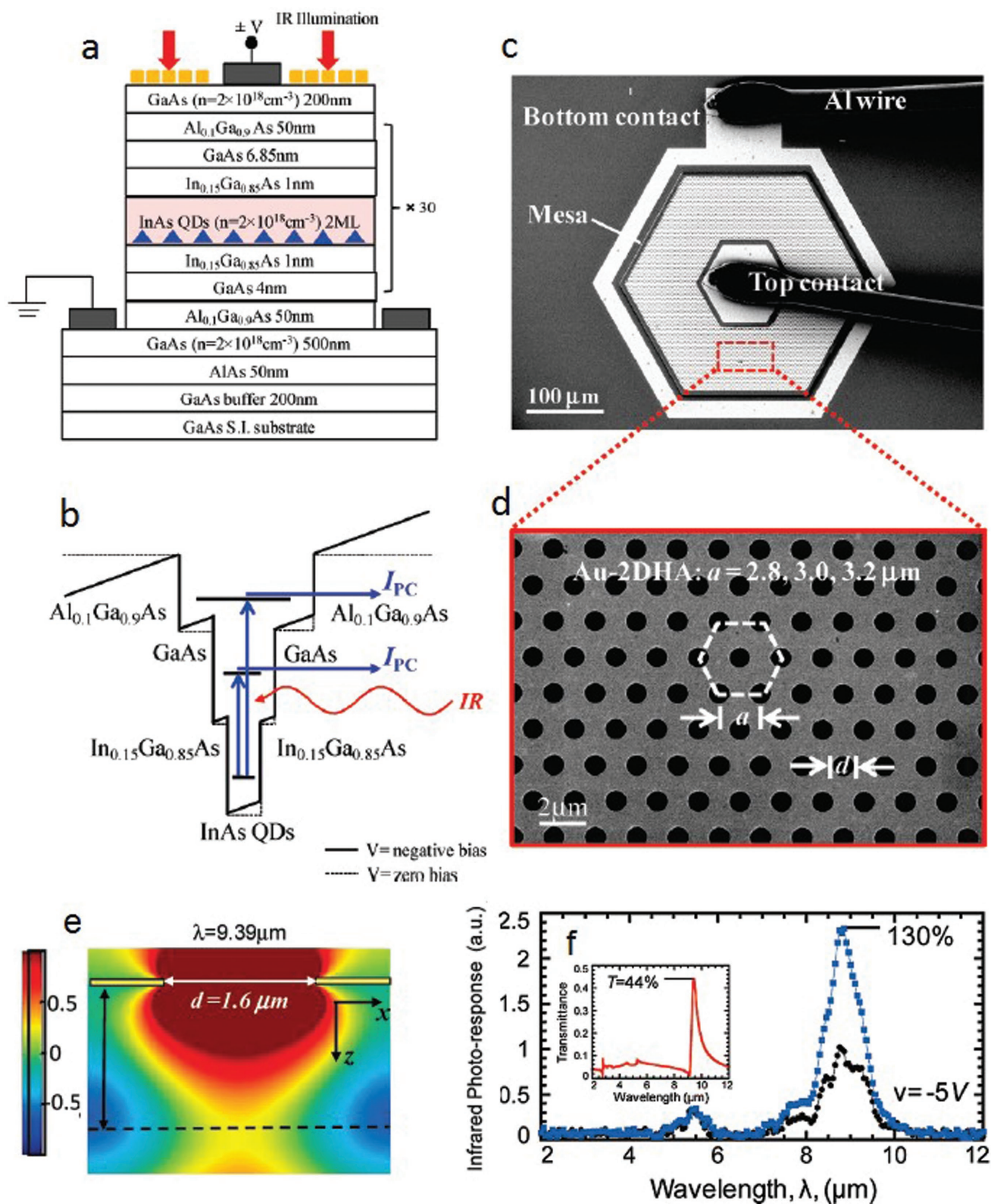


Figure 8. Design of 2D nanohole array on DWELL for enhanced infrared detection. a) Schematic of 30-period DWELL sample structure. b) Schematic energy-band diagram of DWELL structure. The band structure is designed to respond to dual-band infrared excitation at $\lambda = 5$ and $9 \mu\text{m}$. c) Large-area SEM image of the fabricated 2D nanohole array on DWELL device. d) Magnified SEM image of 2D nanohole array. e) FDTD simulated electric field intensity at the Au nanohole. f) Measured photoresponse of the DWELL photodetector with (blue square) and without (black dot) a nanohole array. The inset shows the transmittance of the 2D nanohole array. Reprinted with permission.^[20] Copyright 2010, American Chemical Society.

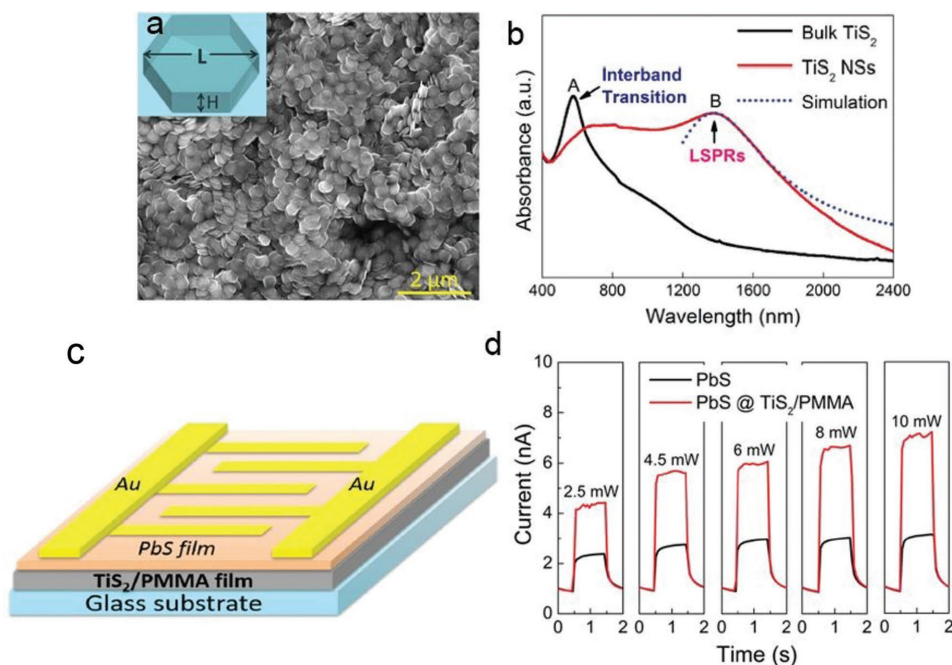


Figure 9. a) SEM image of plasmonic TiS_2 nanoparticles. b) UV-vis-near-infrared (NIR) absorption curve of bulk and TiS_2 nanoparticles. c) Schematics of photodetector geometry with TiS_2 nanoparticles as plasmonic enhancing layer. d) Current-time curves of the PbS film photodetector with and without plasmonic TiS_2 . Reprinted with permission.^[69] Copyright 2016, Wiley.

In addition to the above 1D and 2D photodetectors, plasmonic semiconductor NPs are also proven to be efficient in enhancing the sensitivity of QD-based photodetectors. Zhu et al. recently synthesized plasmonic TiS_2 nanosheets with thicknesses of 6–16 nm and sizes of 180–600 nm (Figure 9a,c).^[69] They tuned the LSPR at $\lambda = 1380$ nm for nanosheets of 16 nm thickness and 300 nm length (Figure 9b), and spin-coated such TiS_2 nanosheet/PMMA films and PbS QD layers on a glass as a near-infrared photodetector. As shown in Figure 9d, the device demonstrated more than twofold enhancement of the photocurrent at $\lambda = 1310$ nm. Likewise, plasmonic titanium nitride NPs were embedded into a photoactive layer of conducting polymerized aniline by physical vapor deposition to make a sensitive photodetector of visible light.^[66] The as-made device exhibited an LSPR at $\lambda = 570$ nm for which a responsivity of 0.57 A W^{-1} and a detectivity of 1.92×10^{11} Jones were demonstrated.

5. LD Plasmonic Photodetectors by Hot-Electron Injection

5.1. Plasmonic Metal-Semiconductor Schottky-Junction Photodetectors

Hot electrons exist as a result of the absorption of the local electromagnetic energy by metal nanoparticles in the nonradiative decay process of LSPR. After scattering with the phonons, they will become the heat dissipation known as Ohmic loss. In fact, hot electrons exist in bulk metals as well as in metal nanostructures.^[70] They were well studied in the IPE of Schottky-junction photodetectors, which, however, exhibits a low efficiency of 0.3–9%.^[16] Plasmonic hot-electron photodetectors have

emerged because the IPE efficiency of the Schottky-junction photodetectors fabricated by plasmonic metal nanostructures can be increased by plasmon-enhanced absorption.^[71] Moreover, Schottky junctions formed between the semiconductors and the metal nanostructures allow sub-bandgap photocurrents due to the IPE of plasmonic hot electrons. As an early example, a TiO_2 thin film that had a bandgap in the UV region was embedded with gold nanoparticles to demonstrate sub-bandgap photodetection. Its enhanced photocurrent spectra peak at 600 nm was close to that of Au NP absorption spectra, which exhibited a resonance band at 600 nm as well. The authors ascribed the impressive change in photoconductance to quantum tunneling of hot electrons from the metal into the conduction band of the TiO_2 , and to energetic electrons going over the barrier transport.^[72]

Later, researchers began to focus more on the IPE efficiency.^[23,73] As elucidated in Figure 10a,b, an Au nanorod array 50 nm in width and 110–158 nm in length was deposited onto n-type Si, onto which silicon dioxide has been previously coated as an insulating layer. The barrier height was 0.5 eV, allowing a detection window of $\lambda = 1.2$ –2.5 μm . By changing the Au nanorod length, the LSPR was tuned from 1250 to 1650 nm, leading to an enhanced IPE efficiency of 2% and a responsivity of 10^{-5} A W^{-1} at $\lambda = 1.25 \mu\text{m}$ (Figure 10c).^[23] Later, comparisons were made of the IPE efficiency between the plasmonic hot-electron photodetectors consisting of a 210 nm wide Au nanograting deposited on top of a n-Si wafer and an Au nanograting embedded in the n-Si at a depth of 25 nm.^[73] The latter enabled a 3D hot-electron injection at three Au-Si interfaces, leading to a 25-fold enhancement of responsivity up to $6 \times 10^{-5} \text{ A W}^{-1}$ at a wavelength of 1.5 μm . Moreover, Knight et al.^[73] used periodically spaced Au slits on the top of the n-Si

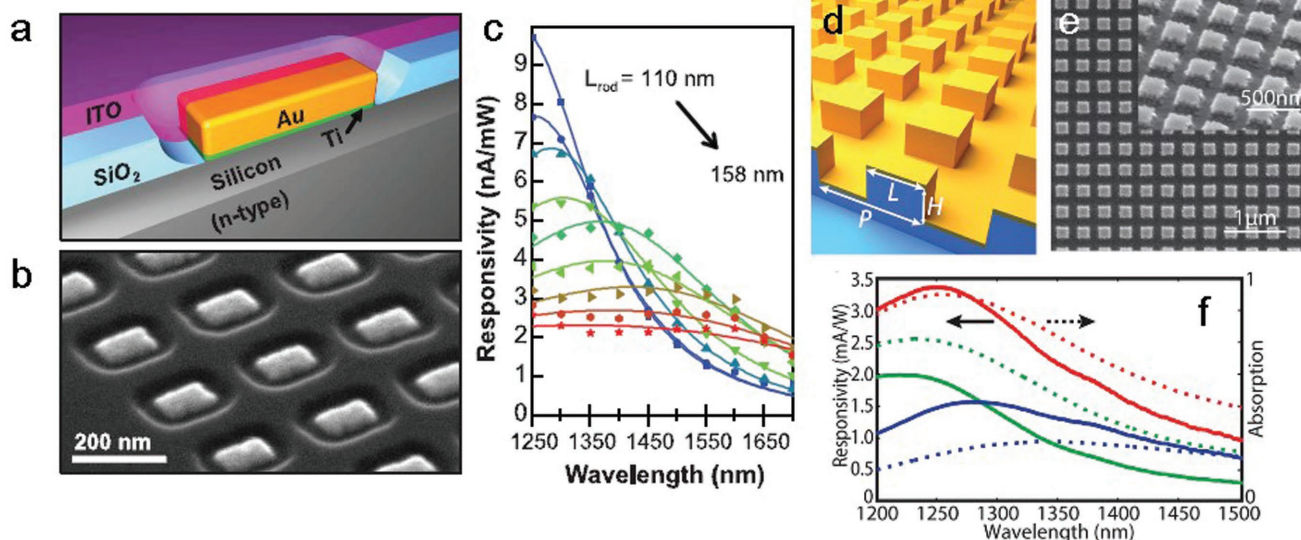


Figure 10. a) Schematic and b) SEM image of Au nanoantenna on n-Si hot-electron photodetector. c) Photoresponse of device with different Au nanorod lengths, the width of the nanorod is 50 nm. d) Schematic, e) SEM image, and f) enhanced responsivity and corresponding absorption resonance of metamaterial perfect absorber. (a–c) Reprinted with permission.^[23] Copyright 2011, American Association for the Advancement of Science. (d–f) Reprinted with permission.^[75] Copyright 2014, American Chemical Society.

to replace the nanograting in the efficient hot-electron photodetector. The slits 200 nm thick, 250 nm wide, and with a period of 1200 nm exhibited extraordinary optical transmission due to the LSPR at $\lambda = 1480$ nm, at which point the responsivity was enhanced to $6 \times 10^{-5} \text{ A W}^{-1}$.^[74]

To further increase the IPE efficiency by enhanced absorption and efficient hot-electron injection, Li and Valentine used a metamaterial perfect absorber that exhibited near 100% absorption.^[75] As shown in Figure 10d,e, the metamaterials consisted of 15 nm thick Au film deposited on the top and bottom of the n-Si nanocube array with tunable sizes. The 15 nm thick Au film was less than the diffusion length of the hot electrons to avoid scattering loss and to ensure efficiency injection. By engineering the nanocube sizes to be 185 nm in length, 160 nm in height, and with periods of 680 nm, the metamaterials exhibited >80% absorption at $\lambda = 1200$ –1500 nm, leading to broadband photodetection with a high responsivity of $3.5 \times 10^{-3} \text{ A W}^{-1}$ (Figure 10f). Furthermore, based on chiral plasmonic metamaterials deposited on n-Si, Li and Valentine demonstrated a novel hot-electron photodetector that is capable of detecting circularly polarized light.^[76]

Lin et al. combined 3D hot-electron injections with a metamaterial perfect absorber by fabricating a deep-trench/thin-metal hot-electron photodetector.^[77] As shown in Figure 11a, a 30 nm thick Au film was deposited onto array of square Si trenches of 650 nm length, 1300 nm periods, and 1200 nm depth. Compared with the Au nanodot and Au nanohole arrays, the LSPR of the Au film in the Si trench was confined in the trench, which leads to an efficient absorption of 80% at $\lambda = 1400$ –1500 nm (Figure 11b,c). The large areas of the gold–Si junction of the trench sidewall allow 3D injection of the hot electrons. Such a combined strategy enabled the device to exhibit a responsivity of $3.8 \times 10^{-3} \text{ A W}^{-1}$. A plasmonic crystal effect for hot-electron detection was also achieved by depositing a 200 nm thick Au film and a 60 nm thick TiO₂ layer on

an ITO square array with a period of 450 nm and a length of 70 nm.^[78] The plasmonic crystal exhibited a tunable LSPR at $\lambda = 400$ –1200 nm, and the device exhibited a highly enhanced responsivity of 70 mA W^{-1} at $\lambda = 640$ nm under a bias of 3 V.

5.2. Plasmonic Metal–Nanomaterial Junction Photodetector

Integrating metal NPs with low-dimensional nanomaterials to form hot-electron photodetectors is emerging not only due to the plasmon-enhanced absorption of the metal NPs, but also due to new phenomena, such as trap-induced internal photogain at the metal/MoS₂ interface.^[6] One of the two electrodes of the MoS₂ hot-electron photodetector should exhibit plasmon-enhanced absorption to generate a net photocurrent.^[79] Valentine and co-workers deposited Au nanowires and Au nanoantennas as the electrodes on a bilayer MoS₂ toward a sensitive hot-electron photodetector.^[80] As shown in Figure 12a–c, the Au nanoantennas exhibited a broad LSPR at $\lambda = 1200$ nm with large forward photocurrent crossing over the Au/MoS₂ barrier of 0.67 eV. The device demonstrated a photoconductive gain of 10^5 and a high responsivity of 5.2 A W^{-1} at $\lambda = 1070$ nm under a bias of 0.6 V (Figure 12d,e). Furthermore, the authors also analyzed the photocurrent generated by the photo-thermoelectric effect at the Au/MoS₂ interface by embedding an aluminum oxide between the Au nanoantenna and the MoS₂ bilayer. It was concluded that the photo-thermoelectric effect is insignificant compared to that of hot-electron injection.

Pescaglioni et al. deposited Au nanorods on a single ZnO nanowire for sub-bandgap hot-electron photodetection over a ZnO/Au Schottky junction with a barrier height of 0.65 eV.^[81] The Au nanorod exhibited LSPR at $\lambda = 650$ nm that led to a 100-fold photocurrent enhancement and an increase of quantum efficiency by $\approx 3\%$. Depositing 100 nm thick aluminum film on a Si pyramid with an apex measuring ≈ 50 nm can also form

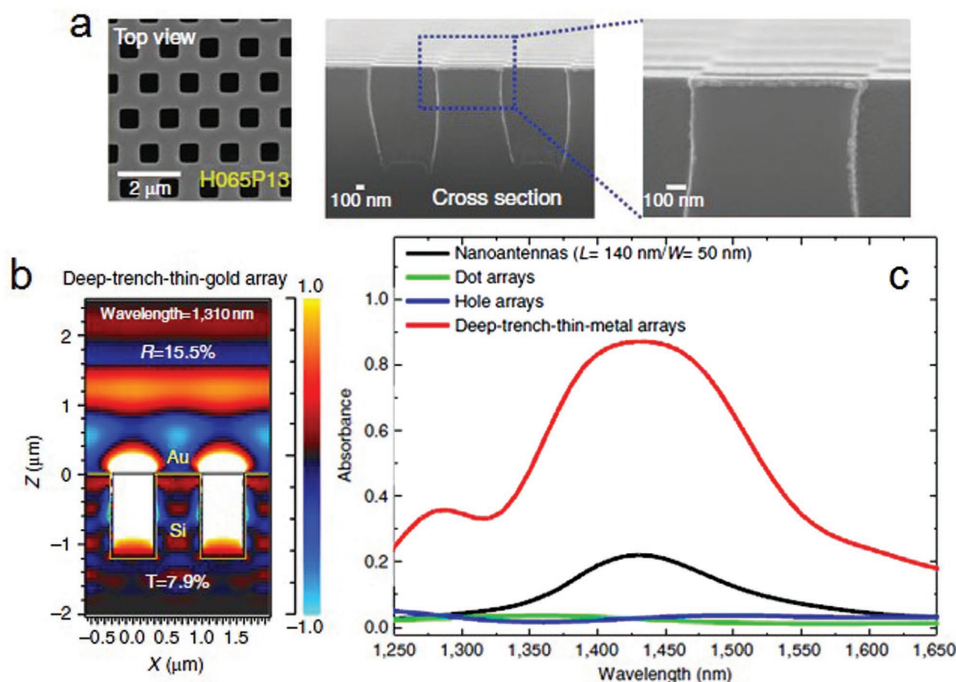


Figure 11. Deep-trench/thin-metal hot-electron photodetector. a) SEM images of the top view and cross-section view of the device. b) FDTD-simulated field distribution of the structure. c) Simulated absorption of four structures in which the deep-trench/thin-metal array exhibits the highest absorption. Reprinted with permission.^[77] Copyright 2014, Nature Publishing Group.

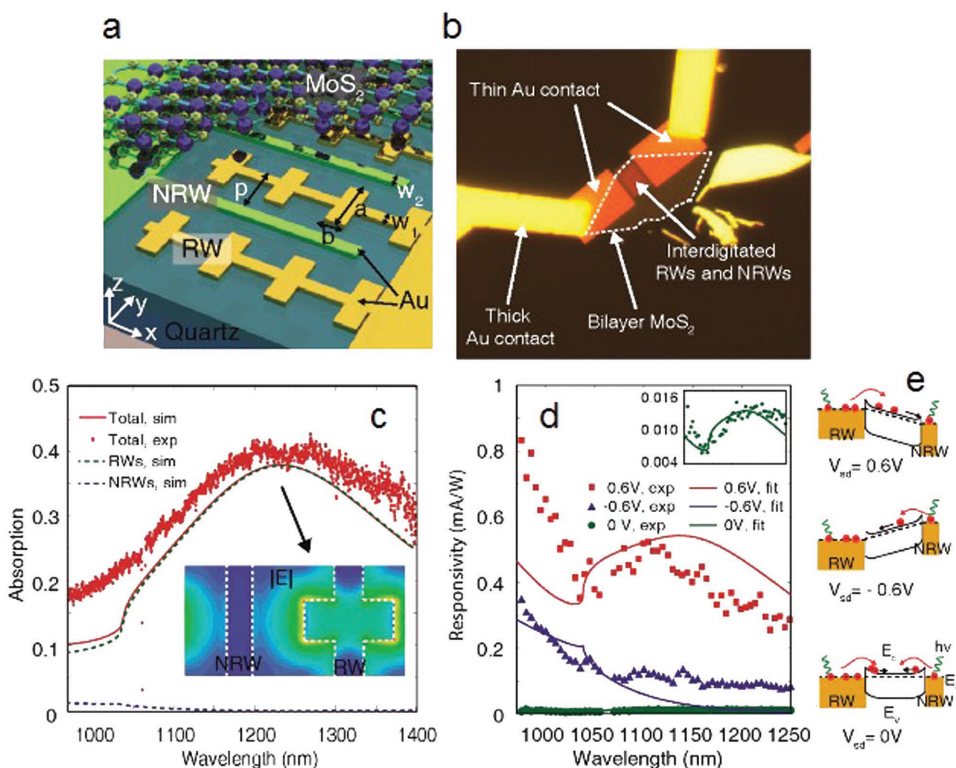


Figure 12. Au resonant nanowire–bilayer MoS₂ plasmonic photodetector: a) Schematic and b) microscopic image of the devices. c) Measured and simulated absorption curves of the device. Inset shows the simulated electric field distribution. d) Measured response under different bias values; inset is a magnified view of the photocurrent at 0 V bias. e) Band diagram of the device under -6, 0, and 6 V bias. Reprinted with permission.^[80] Copyright 2015, American Chemical Society.

a hot-electron photodetector.^[82] The aluminum apex exhibited a plasmonic nanofocusing effect with a 30-fold enhanced electric field confined at the Si pyramid apex at $\lambda = 1300$ nm that led to efficient hot-electron injection. The device exhibited an enhanced responsivity of 30 mA W^{-1} at $\lambda = 1064$ nm with a low dark current of ≈ 100 nA.

6. Conclusions and Outlook

As an important part of a future-integrated nanoscale photonic platform, low-dimensional plasmonic photodetectors allow plasmonic nanoparticles to squeeze light into subdiffraction volumes for absorption enhancement, which continues to benefit from developments in the field of plasmonics. In fact, the life of the nanoparticle LSPR has two sequential stages that could contribute to the photodetection enhancement: (1) the enhanced local electric field, and (2) the increased number of hot electrons due to the enhanced LSP energy absorption by the nanoparticle after the local field has dephased. The former can be used to directly excite more electron-hole pairs of the nearby photogain materials than usual if the LSP energy is higher than the bandgap of the photoelectric materials. Otherwise, the large number of plasmonic hot electrons could be injected into the Schottky junction formed between the nanoparticles and the photogain materials to increase the photocurrent.

2D atomically thin materials, 1D semiconductor nanowires/nanorods, and 0D semiconductor QDs can rely on the plasmon-enhanced local electric field of the metal nanoparticles for direct electron-hole pair excitation. In this regard, two issues should be considered: resonance wavelength matching and spatial overlap. The LSPR depending on the size and shape of the metal nanoparticles should be tuned to match the absorption band of the low-dimensional photogain media. The spatial overlap between the local field and the photogain medium should be optimized for the highest photocurrent enhancement. When semiconductor plasmonic nanoparticles are introduced due to low loss and tunable LSPR wavelength by doping, the photodetectors can be enhanced in the infrared region for biological and communication applications. Finally, the development of the plasmonic hot-electron electrodes with enhanced absorption and small thickness not only improved the performance of the metal-insulator-metal photodetectors, but also expanded the detection spectrum of metal-semiconductor Schottky-junction photodetectors by acquiring sub-bandgap photoelectrons. Together with absorption enhancement, more hot electrons were transported and injected over the Schottky barrier in different configurations of the plasmonic nanostructures.

The development of the low-dimensional plasmonic photodetectors is part of the convergence of nanoscale optoelectronic devices toward nanoscale-integrated photonic systems,^[83] in which the surface-plasmon polariton technology capable of subdiffraction light concentration will play a key role. For example, plasmonic lasers, metal nanowire waveguides, metamaterial flat filters, and plasmonic photodetectors necessary for an integrated sensing chip have been developed,^[84] and, recently, a grating-free nanospectrometer based on plasmonic hot electrons was demonstrated.^[85] While the plasmonic optical

elements were based mostly on metal nanostructures, we foresee that semiconductor nanoparticles will become the trend in plasmonic optoelectronic devices because of their compatibility with existing complementary metal-oxide-semiconductor manufacturing technology. The current nonmetal plasmonic photodetectors were shown to work in the infrared regions, as described in Section 4, although semiconductor materials that could replace Au and Ag to work in the ultraviolet and visible regions are still lacking. Nevertheless, they might be found in the emerging field of 2D atomically thin materials, since intrinsic surface-plasmon polaritons of graphene have been used for infrared photodetection.^[86] Furthermore, perovskite thin film is attracting research attention as a promising photodetection material since its optoelectronic performance has been frequently verified in the field of photovoltaics.^[87] Hybrid perovskite-photodetector-based LD semiconductor materials, as well as plasmonic perovskite photodetectors, are emerging.^[88] As new materials, methods, and mechanisms should appear, we anticipate an exciting field of development, integration, and applications of semiconductor plasmonic photodetectors in the near future.

Acknowledgements

This work was supported by the National Natural Science Foundation of China (NSFC, Nos. 61675062, 61575059, 21501038), the Natural Science Foundation of Anhui Province of China (Nos. 1408085MB31, J2014AKZR0036), and the Fundamental Research Funds for the Central Universities (2013HGCH0012, 2014HGCH0005).

Conflict of Interest

The authors declare no conflict of interest.

Keywords

hot electrons, low-dimensional structures, optoelectronic devices, photodetectors, surface-plasmon resonance

Received: November 27, 2017

Revised: December 28, 2017

Published online:

-
- [1] J. Michel, S. J. Koester, J. Liu, X. Wang, M. W. Geis, S. J. Spector, M. E. Grein, J. U. Yoon, T. M. Lyszczarz, N. N. Feng, in *Handbook of Silicon Photonics* (Eds: L. Vivien, L. Pavesi), CRC Press, Boca Raton, FL, USA **2013**, p. 479.
- [2] a) X. Guo, Y. Ying, L. Tong, *Acc. Chem. Res.* **2014**, *47*, 656; b) F. H. L. Koppens, T. Mueller, P. Avouris, A. C. Ferrari, M. S. Vitiello, M. Polini, *Nat. Nanotechnol.* **2014**, *9*, 780; c) X. Lan, S. Masala, E. H. Sargent, *Nat. Mater.* **2014**, *13*, 233; d) H. Fang, W. Hu, *Adv. Sci.* **2017**, *4*, 1700323; e) H. Wang, J. W. Lim, F. M. Mota, Y. J. Jang, M. Yoon, H. Kim, W. Hu, Y. Y. Noh, D. H. Kim, *J. Mater. Chem. C* **2017**, *5*, 399.
- [3] a) Q. Cui, Y. Yang, J. Li, F. Teng, X. Wang, *Crystals* **2017**, *7*, 149; b) Z. H. Sun, H. X. Chang, *ACS Nano* **2014**, *8*, 4133; c) B. Nie, J. G. Hu, L. B. Luo, C. Xie, L. H. Zeng, P. Lv, F. Z. Li, J. S. Jie,

- M. Feng, C. Y. Wu, Y. Q. Yu, S. H. Yu, *Small* **2013**, *9*, 2872; d) H. Fang, W. Hu, *Sci. China: Phys., Mech. Astron.* **2017**, *60*, 027031; e) J. Wang, H. Fang, X. Wang, X. Chen, W. Lu, W. Hu, *Small* **2017**, *13*, 1700894; f) P. Wang, S. Liu, W. Luo, H. Fang, F. Gong, N. Guo, Z. G. Chen, J. Zou, Y. Huang, X. Zhou, J. Wang, X. Chen, W. Lu, F. Xiu, W. Hu, *Adv. Mater.* **2017**, *29*, 1604439.
- [4] a) S. Li, Y. Liu, H. Y. Hoh, Q. Bao, in *Graphene Photonics, Optoelectronics, and Plasmonics* (Eds: Q. Bao, H. Hoh, Y. Zhang), CRC Press, Boca Raton, FL, USA **2017**, p. 65; b) M. Freitag, T. Low, F. N. Xia, P. Avouris, *Nat. Photonics* **2013**, *7*, 53; c) T. Mueller, F. N. A. Xia, P. Avouris, *Nat. Photonics* **2010**, *4*, 297.
- [5] M. Freitag, T. Low, L. Martin-Moreno, W. J. Zhu, F. Guinea, P. Avouris, *ACS Nano* **2014**, *8*, 8350.
- [6] O. Lopez-Sanchez, D. Lembke, M. Kayci, A. Radenovic, A. Kis, *Nat. Nanotechnol.* **2013**, *8*, 497.
- [7] R. K. Chowdhury, T. K. Sinha, A. K. Katiyar, S. K. Ray, *Nanoscale* **2017**, *9*, 15591.
- [8] a) R. R. LaPierre, M. Robson, K. M. Azizur-Rahman, P. Kuyanov, *J. Phys. D: Appl. Phys.* **2017**, *50*, 123001; b) F. X. Liang, J. Z. Wang, Z. P. Li, L. B. Luo, *Adv. Opt. Mater.* **2017**, *5*, 1700081; c) L. Peng, L. F. Hu, X. S. Fang, *Adv. Mater.* **2013**, *25*, 5321.
- [9] R. V. Shenoi, J. Rosenberg, T. E. Vanderveelde, O. J. Painter, S. Krishna, *IEEE J. Quantum Electron.* **2010**, *46*, 1051.
- [10] M. Y. Chen, L. Shao, S. V. Kershaw, H. Yu, J. F. Wang, A. L. Rogach, N. Zhao, *ACS Nano* **2014**, *8*, 8208.
- [11] L. D. Huang, C. C. Tu, L. Y. Lin, *Appl. Phys. Lett.* **2011**, *98*, 357.
- [12] a) M. Perenzoni, D. J. Paul, in *Physics and Applications of Terahertz Radiation* (Eds: M. Perenzoni, D. J. Paul), Springer, Singapore **2014**; b) A. V. Barve, S. Krishna, in *Advances in Infrared Photodetectors* (Eds: S. D. Gunapala, D. R. Rhyger, C. Jagadish), Elsevier, The Netherlands **2011**; c) M. Razeghi, W. Zhang, H. Lim, S. Tsao, in *Handbook of Self Assembled Semiconductor Nanostructures for Novel Devices in Photonics and Electronics* (Ed: M. Henini), Elsevier, The Netherlands **2008**, p. 620.
- [13] R. R. Nair, P. Blake, A. N. Grigorenko, K. S. Novoselov, T. J. Booth, T. Stauber, N. M. R. Peres, A. K. Geim, *Science* **2008**, *320*, 1308.
- [14] W. L. Barnes, A. Dereux, T. W. Ebbesen, *Nature* **2003**, *424*, 824.
- [15] G. Kumar, P. K. Sarswat, in *Reviews in Plasmonics 2015* (Ed: C. D. Geddes), Springer, Singapore **2016**.
- [16] P. Berini, *Laser Photonics Rev.* **2014**, *8*, 197.
- [17] E. Petryayeva, U. J. Krull, *Anal. Chim. Acta* **2011**, *706*, 8.
- [18] a) R. B. Jiang, B. X. Li, C. H. Fang, J. F. Wang, *Adv. Mater.* **2014**, *26*, 5274; b) J. Gong, G. Li, Z. Tang, *Nano Today* **2012**, *7*, 564; c) C. Clavero, *Nat. Photonics* **2014**, *8*, 95.
- [19] L. B. Luo, X. L. Huang, M. Z. Wang, C. Xie, C. Y. Wu, J. G. Hu, L. Wang, J. A. Huang, *Small* **2014**, *10*, 2645.
- [20] C. C. Chang, Y. D. Sharma, Y. S. Kim, J. A. Bur, R. V. Shenoi, S. Krishna, D. H. Huang, S. Y. Lin, *Nano Lett.* **2010**, *10*, 1704.
- [21] R. Lu, C. W. Ge, Y. F. Zou, K. Zheng, D. D. Wang, T. F. Zhang, L. B. Luo, *Laser Photonics Rev.* **2016**, *10*, 595.
- [22] L. B. Luo, J. J. Chen, M. Z. Wang, H. Hu, C.-Y. Wu, Q. Li, L. Wang, J. A. Huang, F. X. Liang, *Adv. Funct. Mater.* **2014**, *24*, 2794.
- [23] M. W. Knight, H. Sobhani, P. Nordlander, N. J. Halas, *Science* **2011**, *332*, 702.
- [24] A. Comin, L. Manna, *Chem. Soc. Rev.* **2014**, *43*, 3957.
- [25] V. Giannini, A. I. Fernandez-Dominguez, S. C. Heck, S. A. Maier, *Chem. Rev.* **2011**, *111*, 3888.
- [26] C. Sonnichsen, T. Franzl, T. Wilk, G. von Plessen, J. Feldmann, O. Wilson, P. Mulvaney, *Phys. Rev. Lett.* **2002**, *88*, 077402.
- [27] G. V. Hartland, *Chem. Rev.* **2011**, *111*, 3858.
- [28] A. O. Govorov, H. Zhang, H. V. Demir, Y. K. Gun'ko, *Nano Today* **2014**, *9*, 85.
- [29] G. V. Naik, V. M. Shalaev, A. Boltasseva, *Adv. Mater.* **2013**, *25*, 3264.
- [30] A. Pescaglioni, D. Iacopino, *J. Mater. Chem. C* **2015**, *3*, 11785.
- [31] J. D. Hwang, M. J. Lai, H. Z. Chen, M. C. Kao, *IEEE Photonics Technol. Lett.* **2014**, *26*, 1023.
- [32] a) Y. D. Kim, H. Kim, Y. Cho, J. H. Ryoo, C. H. Park, P. Kim, Y. S. Kim, S. Lee, Y. L. Li, S. N. Park, Y. S. Yoo, D. Yoon, V. E. Dorgan, E. Pop, T. F. Heinz, J. Hone, S. H. Chun, H. Cheong, S. W. Lee, M. H. Bae, Y. D. Park, *Nat. Nanotechnol.* **2015**, *10*, 676; b) M. W. Graham, S. F. Shi, D. C. Ralph, J. Park, P. L. McEuen, *Nat. Phys.* **2013**, *9*, 103.
- [33] E. J. H. Lee, K. Balasubramanian, R. T. Weitz, M. Burghard, K. Kern, *Nat. Nanotechnol.* **2008**, *3*, 486.
- [34] Y. Liu, R. Cheng, L. Liao, H. L. Zhou, J. W. Bai, G. Liu, L. X. Liu, Y. Huang, X. F. Duan, *Nat. Commun.* **2011**, *2*, 579.
- [35] T. J. Echtermeyer, L. Britnell, P. K. Jasnós, A. Lombardo, R. V. Gorbachev, A. N. Grigorenko, A. K. Geim, A. C. Ferrari, K. S. Novoselov, *Nat. Commun.* **2011**, *2*, 458.
- [36] a) S. F. Shi, X. D. Xu, D. C. Ralph, P. L. McEuen, *Nano Lett.* **2011**, *11*, 1814; b) M. Freitag, T. Low, W. J. Zhu, H. G. Yan, F. N. Xia, P. Avouris, *Nat. Commun.* **2013**, *4*, 1951; c) L. B. Luo, Y. F. Zou, C. W. Ge, K. Zheng, D. D. Wang, R. Lu, T. F. Zhang, Y. Q. Yu, Z. Y. Guo, *Adv. Opt. Mater.* **2016**, *4*, 763; d) H. Lu, B. P. Cumming, M. Gu, *Opt. Lett.* **2015**, *40*, 3647.
- [37] Z. Y. Fang, Z. Liu, Y. M. Wang, P. M. Ajayan, P. Nordlander, N. J. Halas, *Nano Lett.* **2012**, *12*, 3808.
- [38] W. B. Niu, H. Chen, R. Chen, J. F. Huang, A. Palaniappan, H. D. Sun, B. G. Liedberg, A. I. Y. Tok, *Small* **2014**, *10*, 3637.
- [39] U. J. Kim, S. Yoo, Y. Park, M. Shin, J. Kim, H. Jeong, C. W. Baik, Y. G. Roh, J. Lee, K. Im, H. Son, S. Hwang, C. W. Lee, S. Park, *ACS Photonics* **2015**, *2*, 506.
- [40] Y. Li, J. G. DiStefano, A. A. Murthy, J. D. Cain, E. D. Hanson, Q. Li, F. C. Castro, X. Chen, V. P. Dravid, *ACS Nano* **2017**, *11*, 10321.
- [41] D. D. Wang, C. W. Ge, G. A. Wu, Z. P. Li, J. Z. Wang, T. F. Zhang, Y. Q. Yu, L. B. Luo, *J. Mater. Chem. C* **2017**, *5*, 1328.
- [42] Y. Wang, C. W. Ge, Y. F. Zou, R. Lu, K. Zheng, T. F. Zhang, Y. Q. Yu, L. B. Luo, *Adv. Opt. Mater.* **2016**, *4*, 291.
- [43] J. F. Lu, C. X. Xu, J. Dai, J. T. Li, Y. Y. Wang, Y. Lin, P. L. Li, *Nanoscale* **2015**, *7*, 3396.
- [44] a) X. Zhang, Q. Liu, B. Liu, W. Yang, J. Li, P. Niu, X. Jiang, *J. Mater. Chem. C* **2017**, *5*, 4319; b) P. Biswas, S. R. Cho, J.-W. Kim, S. D. Baek, J.-M. Myoung, *Nanotechnology* **2017**, *28*, 225502.
- [45] L. Wang, X. Ma, R. Chen, Y. Q. Yu, L. B. Luo, *J. Mater. Sci.: Mater. Electron.* **2015**, *26*, 4290.
- [46] L. Wang, R. Chen, Z. F. Ren, C. W. Ge, Z. X. Liu, S. J. He, Y. Q. Yu, C. Y. Wu, L. B. Luo, *Nanotechnology* **2016**, *27*, 215202.
- [47] L. B. Luo, K. Zheng, C. W. Ge, Y. F. Zou, R. Lu, Y. Wang, D. D. Wang, T. F. Zhang, F. X. Liang, *Plasmonics* **2016**, *11*, 619.
- [48] L. B. Luo, W. J. Xie, Y. F. Zou, Y. Q. Yu, F. X. Liang, Z. J. Huang, K. Y. Zhou, *Opt. Express* **2015**, *23*, 12979.
- [49] L. B. Luo, L. H. Zeng, C. Xie, Y. Q. Yu, F. X. Liang, C. Y. Wu, L. Wang, J. G. Hu, *Sci. Rep.* **2014**, *4*, 3914.
- [50] F. X. Liang, C. W. Ge, T. F. Zhang, W. J. Xie, D. Y. Zhang, Y. F. Zou, Z. Kun, L. B. Luo, *Nanophotonics* **2017**, *6*, 494.
- [51] S. Alkis, F. B. Oruc, B. Ortac, A. C. Kosger, A. K. Okyay, *J. Opt.* **2012**, *14*, 125001.
- [52] F. J. Beck, A. Stavrinadis, S. L. Diedenhofen, T. Lasanta, G. Konstantatos, *ACS Photonics* **2014**, *1*, 1197.
- [53] J. Kern, A. Trugler, I. Niehues, J. Ewering, R. Schmidt, R. Schneider, S. Najmaei, A. George, J. Zhang, J. Lou, U. Hohenester, S. M. de Vasconcellos, R. Bratschkitsch, *ACS Photonics* **2015**, *2*, 1260.
- [54] S. D. Lei, F. F. Wen, L. H. Ge, S. Najmaei, A. George, Y. J. Gong, W. L. Gao, Z. H. Jin, B. Li, J. Lou, J. Kono, R. Vajtai, P. Ajayan, N. J. Halas, *Nano Lett.* **2015**, *15*, 3048.
- [55] a) W. Choi, M. Y. Cho, A. Konar, J. H. Lee, G. B. Cha, S. C. Hong, S. Kim, J. Kim, D. Jena, J. Joo, *Adv. Mater.* **2012**, *24*, 5832; b) H. S. Lee, S. W. Min, Y. G. Chang, M. K. Park, T. Nam, H. Kim,

- J. H. Kim, S. Ryu, S. Im, *Nano Lett.* **2012**, *12*, 3695; c) Z. Y. Yin, H. Li, L. Jiang, Y. M. Shi, Y. H. Sun, G. Lu, Q. Zhang, X. D. Chen, H. Zhang, *ACS Nano* **2012**, *6*, 74.
- [56] S. D. Lei, L. H. Ge, S. Najmaei, A. George, R. Kappera, J. Lou, M. Chhowalla, H. Yamaguchi, G. Gupta, R. Vajtai, A. D. Mohite, P. M. Ajayan, *ACS Nano* **2014**, *8*, 1263.
- [57] K. M. Goodfellow, C. Chakraborty, R. Beams, L. Novotny, A. N. Vamiryakas, *Nano Lett.* **2015**, *15*, 5477.
- [58] J. S. Miao, W. D. Hu, Y. L. Jing, W. J. Luo, L. Liao, A. L. Pan, S. W. Wu, J. X. Cheng, X. S. Chen, W. Lu, *Small* **2015**, *11*, 2392.
- [59] Y. H. Zhan, X. F. Li, D. Y. Lei, S. L. Wu, C. H. Wang, Y. Li, *ACS Photonics* **2014**, *1*, 483.
- [60] L. Lin, G. Q. Gao, Q. Zhu, A. W. Xu, *J. Mater. Chem. A* **2015**, *3*, 12845.
- [61] S. B. Wang, R. S. Chen, S. J. Chang, H. C. Han, M. S. Hu, K. H. Chen, L. C. Chen, *Nanoscale* **2014**, *6*, 1264.
- [62] a) D. S. Choi, M. Hansen, E. Van Keuren, J. I. Hahm, *Nanotechnology* **2017**, *28*, 145203; b) Z. Zhu, Y. Gu, S. Wang, Y. Zou, H. Zeng, *Adv. Electron. Mater.* **2017**, *3*, 1700281.
- [63] P. Senanayake, C. H. Hung, A. Farrell, D. A. Ramirez, J. Shapiro, C. K. Li, Y. R. Wu, M. M. Hayat, D. L. Huffaker, *Nano Lett.* **2012**, *12*, 6448.
- [64] P. Senanayake, C. H. Hung, J. Shapiro, A. Lin, B. L. Liang, B. S. Williams, D. L. Huffaker, *Nano Lett.* **2011**, *11*, 5279.
- [65] Z. Ku, W. Y. Jang, J. F. Zhou, J. O. Kim, A. V. Barve, S. Silva, S. Krishna, S. R. J. Brueck, R. Nelson, A. Urbas, S. Kang, S. J. Lee, *Opt. Express* **2013**, *21*, 4709.
- [66] S. J. Lee, Z. Y. Ku, A. Barve, J. Montoya, W. Y. Jang, S. R. J. Brueck, M. Sundaram, A. Reisinger, S. Krishna, S. K. Noh, *Nat. Commun.* **2011**, *2*, 286.
- [67] a) X. Liu, M. T. Swihart, *Chem. Soc. Rev.* **2014**, *43*, 3908; b) P. R. West, S. Ishii, G. V. Naik, N. K. Emani, V. M. Shalaev, A. Boltasseva, *Laser Photonics Rev.* **2010**, *4*, 795; c) Z. Ni, L. Ma, S. Du, Y. Xu, M. Yuan, H. Fang, Z. Wang, M. Xu, D. Li, J. Yang, W. Hu, X. Pi, D. Yang, *ACS Nano* **2017**, *11*, 9854.
- [68] T. Sun, Y. Wang, W. Yu, Y. Wang, Z. Dai, Z. Liu, B. N. Shivananju, Y. Zhang, K. Fu, B. Shabbir, *Small* **2017**, *13*, 1701881.
- [69] Z. F. Zhu, Y. S. Zou, W. D. Hu, Y. B. Li, Y. Gu, B. Q. Cao, N. Guo, L. Wang, J. Z. Song, S. L. Zhang, H. S. Gu, H. B. Zeng, *Adv. Funct. Mater.* **2016**, *26*, 1793.
- [70] a) C. Zhang, K. Wu, V. Giannini, X. Li, *ACS Nano* **2017**, *11*, 1719; b) K. Wu, Y. Zhan, C. Zhang, S. Wu, X. Li, *Sci. Rep.* **2015**, *5*, 14304.
- [71] K. Wu, Y. H. Zhan, S. L. Wu, J. J. Deng, X. F. Li, *J. Appl. Phys.* **2015**, *118*, 063101.
- [72] S. Mubeen, G. Hernandez-Sosa, D. Moses, J. Lee, M. Moskovits, *Nano Lett.* **2011**, *11*, 5548.
- [73] M. W. Knight, Y. M. Wang, A. S. Urban, A. Sobhani, B. Y. Zheng, P. Nordlander, N. J. Halas, *Nano Lett.* **2013**, *13*, 1687.
- [74] A. Sobhani, M. W. Knight, Y. M. Wang, B. Zheng, N. S. King, L. V. Brown, Z. Y. Fang, P. Nordlander, N. J. Halas, *Nat. Commun.* **2013**, *4*, 2642.
- [75] W. Li, J. Valentine, *Nano Lett.* **2014**, *14*, 3510.
- [76] W. Li, Z. J. Coppens, L. V. Besteiro, W. Y. Wang, A. O. Govorov, J. Valentine, *Nat. Commun.* **2015**, *6*, 8379.
- [77] K. T. Lin, H. L. Chen, Y. S. Lai, C. C. Yu, *Nat. Commun.* **2014**, *5*, 3288.
- [78] F. P. G. de Arguer, A. Mihi, G. Konstantatos, *ACS Photonics* **2015**, *2*, 950.
- [79] T. Hong, B. Chamlagain, S. R. Hu, S. M. Weiss, Z. X. Zhou, Y. Q. Xu, *ACS Nano* **2015**, *9*, 5357.
- [80] W. Y. Wang, A. Klots, D. Prasai, Y. M. Yang, K. I. Bolotin, J. Valentine, *Nano Lett.* **2015**, *15*, 7440.
- [81] A. Pescaglini, A. Martin, D. Cammi, G. Juska, C. Ronning, E. Pelucchi, D. Iacopino, *Nano Lett.* **2014**, *14*, 6202.
- [82] B. Desiatov, I. Goykhman, N. Mazurski, J. Shappir, J. B. Khurgin, U. Levy, *Optica* **2015**, *2*, 335.
- [83] M. Tchernycheva, A. Messanvi, A. D. Bugallo, G. Jacopin, P. Lavenus, L. Rigutti, H. Zhang, Y. Halioua, F. H. Julien, J. Eymery, C. Durand, *Nano Lett.* **2014**, *14*, 3515.
- [84] A. F. Koenderink, A. Alu, A. Polman, *Science* **2015**, *348*, 516.
- [85] F. M. Wang, N. A. Melosh, *Nat. Commun.* **2013**, *4*, 1711.
- [86] a) Q. Xu, Y. Lu, J. Yuan, Y. Zhang, Q. Bao, in *Graphene Photonics, Optoelectronics, and Plasmonics* (Eds: Q. Bao, H. Hoh, Y. Zhang), CRC Press, Boca Raton, FL, USA **2017**, p. 101; b) F. J. Garcia de Abajo, *ACS Photonics* **2014**, *1*, 135; c) Q. Bao, K. P. Loh, *ACS Nano* **2012**, *6*, 3677.
- [87] a) J. W. Lee, H. S. Kim, N. G. Park, *Acc. Chem. Res.* **2016**, *49*, 311; b) Q. Lin, A. Armin, P. L. Burn, P. Meredith, *Acc. Chem. Res.* **2016**, *49*, 545; c) S. Chen, G. Shi, *Adv. Mater.* **2017**, *29*, 1605448; d) Y. Zhao, K. Zhu, *Chem. Soc. Rev.* **2016**, *45*, 655.
- [88] a) X. W. Tong, W. Y. Kong, Y. Y. Wang, J.-M. Zhu, L. B. Luo, Z. H. Wang, *ACS Appl. Mater. Interfaces* **2017**, *9*, 18977; b) W. Zheng, R. Lin, Z. Zhang, Q. Liao, J. Liu, F. Huang, *Nanoscale* **2017**, *9*, 12718; c) Y. Dong, Y. Gu, Y. Zou, J. Song, L. Xu, J. Li, F. Xue, X. Li, H. Zeng, *Small* **2016**, *12*, 5622; d) J. Lu, A. Carvalho, H. Liu, S. X. Lim, A. H. Castro Neto, C. H. Sow, *Angew. Chem., Int. Ed.* **2016**, *55*, 11945; e) Z. Sun, L. Aigouy, Z. Chen, *Nanoscale* **2016**, *8*, 7377; f) L. Lv, Y. Xu, H. Fang, W. Luo, F. Xu, L. Liu, B. Wang, X. Zhang, D. Yang, W. Hu, A. Dong, *Nanoscale* **2016**, *8*, 13589.